Astronomy & Astrophysics manuscript no. n2hp_mapping
January 9, 2014

Kinematic structure of massive star-forming regions - I. Accretion along filaments

J. Tackenberg[1], H. Beuther[1], Th. Henning[1], H. Linz[1], T. Sakai[2], S. E. Ragan[1], O. Krause[1], M. Nielbock[1], M. Hennemann[1,3], J. Pitann[1], A. Schmiedeke[1,4]

[1] Max-Planck-Institut für Astronomie (MPIA), Königstuhl 17, 69117 Heidelberg, Germany
e-mail: last-name@mpia.de
[2] Graduate School of Informatics and Engineering, The University of Electro-Communications, Chofu, Tokyo 182-8585, Japan
[3] AIM Paris-Saclay, CEA/DSM/IRFU – CNRS/INSU – Université Paris Diderot, CEA Saclay, 91191 Gif-sur-Yvette cedex, France
[4] Universität zu Köln, Zülpicher Str. 77, 50937, Köln, Germany

Received September 15, 1996; accepted March 16, 1997

ABSTRACT

Context. The mid- and far-infrared view on high-mass star formation, in particular with the results from the *Herschel* space observatory, has shed light on many aspects of massive star formation. However, these continuum studies lack kinematic information.
Aims. We study the kinematics of the molecular gas in high-mass star-forming regions.
Methods. We complement the PACS and SPIRE far-infrared data of 16 high-mass star-forming regions from the *Herschel* Key project EPoS with N_2H^+ molecular line data from the MOPRA and Nobeyama 45m telescope. Using the full N_2H^+ hyperfine structure, we produce column density, velocity, and linewidth maps. These are correlated with PACS 70 μm images and PACS point sources. In addition, we search for velocity gradients.
Results. For several regions, the data suggest that the linewidth on the scale of clumps is dominated by outflows or unresolved velocity gradients. IRDC 18454 and G11.11 show two velocity components along several line-of-sights. We find that all regions with a diameter larger than 1 pc show either velocity gradients or fragment into independent structures with distinct velocities. The velocity profiles of 3 regions with a smooth gradient are consistent with gas flows along the filament, suggesting accretion flows onto the densest regions.
Conclusions. We show that the kinematics of several regions show significant and complex velocity structure. For three filaments, we suggest that gas flows toward the more massive clumps are present.

Key words. Stars:formation, kinematics and dynamics

1. Introduction

Despite their rarity, high-mass stars are important for all fields of astronomy. Within the Milky Way they shape and regulate the formation of clusters, influence the chemistry of the interstellar medium, and might have even affected the formation of the solar system (Gritschneder et al. 2012). On the larger scales, emission from high-mass stars dominates the emission detected from external galaxies. In addition, massive stars are the origin of heavy elements on all scales. Nevertheless, high-mass star formation is far from understood (Beuther et al. 2007; Zinnecker & Yorke 2007).

Sensitive IR and (sub-) mm Galactic plane surveys together with results from the *Herschel*[1] space observatory (Pilbratt et al. 2010) have shed new light on the cradles of massive stars/clusters and their early formation. Perault et al. (1996) and Egan et al. (1998) discovered extinction patches in the bright mid-IR background using the ISO (Kessler et al. 1996) and MSX (Egan et al. 2003) satellites, similar to the dark patches reported by Barnard (1919) which are today known to be connected to low-mass star formation. Soon after, Carey et al. (1998) established the so-called infrared dark clouds (IRDCs) as precursors of high-mass star formation. Today, the Spitzer observatory Galactic plane surveys GLIMPSE at 3.6 μm, 4.5 μm, 5.8 μm, and 8 μm (Benjamin et al. 2003), and MIPSGAL at 24 μm (Carey et al. 2009) allow the systematic search for IRDCs with unprecedented sensitivity (e.g. Peretto & Fuller 2009).

While Spitzer improved our mid-IR view of the Galaxy, the *Herschel* satellite allows observations of the far-IR. With the PACS (Poglitsch et al. 2010) and SPIRE (Griffin et al. 2010) photometer, high sensitivity and spatial resolution observations between 70 μm and 500 μm are possible. From correlating data at mid-IR through sub-millimeter and millimeter wavelengths, the picture emerged that most star-forming regions are filamentary (André et al. 2010; Men'shchikov et al. 2010; Molinari et al. 2010; Schneider et al. 2010; Hill et al. 2011; Hennemann et al. 2012; Peretto et al. 2012).

In numerical studies, the formation of dense cores and clumps is explained by two scenarios. On the one hand, molecular clouds fragment in a self-similar cascade down to the typical size of dense, quasi-static cores supported by turbulence. These will then form single or multiple gravitationally bound objects (McKee & Tan 2003; Zinnecker & Yorke 2007). On the other hand, in the dynamical theory molecular clouds are formed from large-scale flows of atomic gas as transient objects (Mac Low & Klessen 2004; Klessen et al. 2005; Heitsch & Hartmann 2008; Clark et al. 2012). Within these transient structures, su-

[1] *Herschel* is an ESA space observatory with science instruments provided by European-led Principal Investigator consortia and with important participation from NASA.

personic turbulence compresses some fraction of the gas to filaments, clumps, and dense cores. If gravity dominates, the cores collapse. In contrast to the quasi-static cores, these cores constantly grow in mass. If, by chance, some cores accrete mass faster than others due to their higher initial gravitational potential, this is called competitive accretion (Bonnell et al. 2004). Also dynamical, but of reversed reasoning, in the fragmentation-induced starvation scenario by Peters et al. (2010), individual massive dense cores build from the large-scale flows, and an accompanying cluster of smaller cores drag away material from the main core and diminish its mass accretion.

The Earliest Phases of Star formation (EPoS, PI O. Krause) is a Guaranteed Time *Herschel* Key Program for investigating 14 low-mass and 45 high-mass star-forming regions. The low-mass observations have been summarized in Launhardt et al. (2013), and the high-mass part has been described in Ragan et al. (2012a). The high-mass part of the project provides an excellent target list for studying the kinematics in star-forming regions. This is the ultimate goal of this paper, using N_2H^+ molecular line data.

2. Observations and analysis

2.1. EPoS - A *Herschel* Key Project

All 45 high-mass EPoS sources were observed with the *Herschel* satellite (Pilbratt et al. 2010) at 70 μm, 100 μm, 160 μm, 250 μm, 350 μm, and 500 μm with a spatial resolution of 5.6″, 6.8″, 11.3″, 18.1″, 25.2″, and 36.6″, respectively (Poglitsch et al. 2010; Griffin et al. 2010). The observations were performed in two orthogonal directions and the data reduction has been performed using *HIPE* (Ott 2010) and *scanamorphos* (Roussel 2012). A more detailed description of the data reduction is given in Ragan et al. (2012a).

Out of the 45 *Herschel* EPoS high-mass sources we selected a sub-sample of 17 regions given in Table 1 that cover each important evolutionary stage: promising high-mass starless core candidates, IRDCs with weak mid- and far-infrared sources, indicative of early ongoing star formation activity, and known high-mass protostellar objects (HMPOs).

The protostellar core population was already characterized in Ragan et al. (2012a) using *Herschel* photometry, supplemented by Spitzer, IRAS, and MSX data. By modeling the spectral energy distributions (SEDs), the authors fit the temperature, luminosity, and mass of each protostellar core in the sample.

2.2. Nobeyama 45m observations

Between April 7th and 12th 2010 the BEam Array Receiver System (BEARS, Sunada et al. 2000) on the Nobeyama Radio Observatory (NRO[2]) 45 m telescope was used to map six of the regions in N_2H^+; the details are given in Table 1. At a frequency of the N_2H^+ (1-0) transition of 93.173 GHz, the spatial resolution of the NRO 45 m telescope is 18″(HPBW) and the observing mode with a band-width of 32 MHz has a frequency resolution of 62.5 kHz, or 0.2 km/s. All observations were performed using on-the-fly (OTF) mapping in varying weather conditions, with an average system temperature of 280 K and high precipitable water vapors between 3 mm and 9 mm. The pointing was done using the single pixel receiver S40 tuned to SiO. As pointing sources we used the SiO masers of the late-type stars V468 Cyg, IRC+00363, and R Aql. Although the wind conditions contributed to the pointing uncertainties, the pointing is better than a third of the beam.

For the data reduction we used NOSTAR (Sawada et al. 2008), a software package provided by the NRO for OTF data. The data is sampled to a spatial grid of 7.5″and smoothed to a spectral resolution of 0.5 km/s. To account for the different efficiencies of the 25 receivers in the BEARS array we corrected each pixel to the efficiency of the S100 receiver, using individual correction factors and a beam efficiency of $\eta = 0.46$ to calculate main-beam temperatures. The noisy edges due to less coverage have been removed within NOSTAR by suppressing pixels in the final maps with a rms noise above 0.15 K. The resulting antenna temperature maps have an average rms noise between 0.12 K and 0.13 K per beam.

2.3. MOPRA observations

11 sources, listed in Table 1, were mapped with the 22 m MOPRA radio telescope, operated by the Australia Telescope National Facility (ATNF) in OTF mode. The observations were carried out in 2010, June 1st to 5th and 25th to 27th, as well as July 7th through 9th. High precipitable water vapors during the observations result in system temperatures mostly between 200 K and 300 K. Observations with system temperatures above 500 K were ignored during the data reduction.

We employed 13 of the MOPRA spectrometer (MOPS) zoom bands, each of 138 MHz width and 4096 channels, resulting in a velocity resolution of 0.11 km/s at 90 GHz. The spectral setup covered transitions of CH_3CCH, $H^{13}CN$, $H^{13}CO^+$, SiO, C_2H, HNCO, HCN, HCO^+, HNC, HCCCN, CH_3CN, ^{13}CS, and N_2H^+ in the 90 GHz regime (for details on the transitions and their excitation conditions see Vasyunina et al. 2011). At this wavelength, the MOPRA beam FWHM is 35.5″and the beam efficiency is assumed to be constant over the frequency range with $\eta = 0.49$ (Ladd et al. 2005). The data reduction was done using LIVEDATA and GRIDZILLA, an on-the-fly mapping analysis package provided by the ATNF. In order to improve the signal-to-noise ratio we spatially smoothed the data to a beam FWHM of 46″within (and as suggested by) *gridzilla*. The final maps were smoothed to a spectral resolution of 0.21 km/s - 0.23 km/s (depending on the transition frequency). Spectra with an rms noise above 0.12 K have been removed, affecting pixels at the edges. The resulting average rms noise of the individual maps is then below 0.09 K/beam.

However, the observed regions of interest are dense but still cold. Therefore, with the achieved sensitivity at the given spatial resolution we do not detect the more complex or low-abundance molecules. For example, although SiO (2-1) has been detected toward several positions that we have mapped (Sridharan et al. 2002; Sakai et al. 2010), the strongest SiO emitter found by Linz et al. (in prep., G28.34-2) is at our noise level and therefore not detected. Commonly detected and reasonably mapped are HCN (1-0), HNC (1-0), HCO^+ (1-0), $H^{13}CO^+$ (1-0), and N_2H^+ (1-0). As we discuss in Sect. 2.5, we concentrate on N_2H^+, a well known cold dense gas tracer.

2.4. Dust continuum

In order to trace the total cold gas we use the cold dust emission as a tracer of the molecular gas. As most of the selected sources lie within the Galactic plane, the APEX 870 μm survey ATLASGAL (Schuller et al. 2009; Contreras et al. 2013) cov-

[2] Nobeyama Radio Observatory is a branch of the National Astronomical Observatory of Japan, National Institutes of Natural Sciences.

Table 1. Observed IRDCs.

Source name	RA(J2000) [hh mm ss.s]	DEC(J2000) [dd:mm:ss]	Gal. longitude [°]	Gal. latitude [°]	Distance [kpc]	**beam size** [pc]	minimum N_2H^+ detection $\times 10^{12}$ cm^{-2}	minimum N_2H^+ detection 0.4 km/s $\times 10^{12}$ cm^{-2}
Observed with Nobeyama 45m								
IRDC 18223	18 25 10.7	-12 45 12	18.613	-0.081	3.5	0.3	0.8	
IRDC 18310	18 33 44.7	-08 22 36	23.467	0.085	4.9	0.4	3.9	
IRDC 18385	18 41 17.1	-05 09 15	27.189	-0.098	3.1	0.3	1.2	
IRDC 18454	18 47 58.1	-01 54 41	30.835	-0.100	5.3	0.5	4.1	
ISOSS J20153	20 15 21.4	+34 53 52	72.953	-0.027	1.2	0.1	8.1	
IRDC 13.90	18 17 26.1	-17 05 26	13.906	-0.473	2.6	0.2	1.4	
Observed with Mopra								
IRDC 18102	18 13 12.2	-17 59 34	12.632	-0.016	2.6	0.6	5.7	3.3
IRDC 18151	18 17 55.3	-12 07 29	18.335	1.778	2.7	0.6	3.9	2.8
IRDC 18182	18 21 12.2	-14 32 46	16.577	-0.069	3.4	0.7	3.2	2.2
IRDC 18306	18 33 29.9	-08 32 07	23.298	0.066	3.6	0.8	1.5	1.6
IRDC 18308	18 33 33.1	-08 37 46	23.220	0.011	4.4	1.0	2.9	2.1
IRDC 18337	18 36 29.6	-07 40 33	24.402	-0.197	3.7	0.8	1.8	1.1
IRDC 19.30	18 25 58.1	-12 05 09	19.293	0.060	2.4	0.5	7.6	1.3
IRDC 11.11	18 10 20.0	-19 25 05	11.056	-0.107	3.4	0.7	2.4	1.6
IRDC 15.05	18 17 40.4	-15 49 12	15.052	0.080	3.0	0.7	3.4	1.4
IRDC 28.34	18 42 48.1	-04 01 51	28.361	0.080	4.5	1.0	4.5	3.2
IRDC 48.66	19 21 40.7	+13 50 32	48.666	-0.263	2.6	0.6	2.3	0.8

Position columns (2-5) give the center coordinate of the maps. The actual areas that have been mapped are displayed in Fig. 1 through Fig. 4. The distances are adopted from (Ragan et al. 2012a) with references therein. The detected N_2H^+ minimum the minimum plotted in Fig. 1 through Fig. 4. For sources observed with MOPRA we also give the improved minimum detection when smoothing the spectra to a velocity resolution of 0.4 km/s. Also observed with the NRO 45m telescope but not detected have been IRDC20081, ISOSSJ19357, ISOSSJ19557, and ISOSSJ20093.

ers all but two sources. Its beam size is 19.2″and its average rms noise is 50 mJy/beam. IRDC 18151 with a Galactic latitude of ∼ 1.7°is not covered by ATLASGAL. Instead we use IRAM 30 m MAMBO data (Beuther et al. 2002b). At a wavelength of 1.2 mm, the beam width is 10.5″, and the rms noise in the dust map is 17 mJy/beam. In addition, ISOSS J20153 is outside the coverage of ATLASGAL. Here we used 850 μm data from the SCUBA camera at the JCMT[3] (Hennemann et al. 2008). The beam width is 14″and the rms noise 14 mJy/beam. A summary of the properties of the sub-mm data is given in Table 2.

2.5. N_2H^+ hyperfine fitting

Our molecular line study focuses on the N_2H^+ J=1-0 line as dense molecular gas tracer. Using the Einstein A and collison coefficient for a temperature of 20 K (Schöier et al. 2005), its critical density is 1.6×10^5 cm^{-3}, and its hyperfine structure allows one to reliably measure its optical depth and thus the distribution over a wide range of densities. In addition, the velocity and linewidth can be measured without being affected by optical depth effects. Finally, it is detected toward both low- and high-mass star-forming regions of various evolutionary stages (Schlingman et al. 2011). Therefore, it is well suited for studies of young high-mass star-forming regions.

To extract the N_2H^+ line parameters, we fit a N_2H^+ hyperfine structure to each pixel using *class* from the *GILDAS*[4] package. For every spectrum we calculate the rms and the peak intensity of the brightest component derived from the fit parameters. If the peak is higher than three times the rms value, the fit parameters peak velocity, and linewidth together with an integrated intensity are stored to a parameter map. Otherwise, the pixel is left blank. The low detection threshold of 3 σ is justified for two reasons. (1) For only a very limited number of pixels that fulfill the 3 σ criterion, the fitted line-width is twice the channel width or less. Therefore, introducing an additional check on the integrated intensity, e.g. a 5 σ, does not improve the fit reliability. (2) The resulting parameter maps show only smooth transition in each parameter relative to neighboring pixels. For the same pixels, smoothing over a larger area would increase the signal to noise but worsen the resolution. Therefore, the small scale structure would be lost. For our purposes, fitting the hyperfine structure even in low signal-to-noise maps provides reliable results.

From the integrated intensity ($\int T_{mb}$), determined as the sum over channels times the channel width, and the fitted optical depth τ, we calculated the column densities of N_2H^+. We used the formula from Tielens (2005),

$$N_J = 1.94 \times 10^3 \frac{\nu^2 \int T_{mb}}{A_u} \times \frac{\tau}{1 - e^{\tau}} \text{ (for J+1 to J)} \quad (1)$$

$$N_{tot} = \frac{Q}{g_u} \times N_J \times e^{E_u/kT_{ex}}, \quad (2)$$

where N_J is the number of molecules in the the J-th level, and N_{tot} the total number of molecules. A_u is the Einstein A coefficient of the upper level, E_u/k is the excitation energy of the upper level in K, both adopted from Schöier et al. (2005); Vasyunina et al. (2011); Q is the partition function of the given level, taken from the Cologne Database for Molecular Spectroscopy (Müller et al. 2005); g_u is the degeneracy of the energy level.

[3] *The James Clerk Maxwell Telescope* is operated by the Joint Astronomy Centre on behalf of the Particle Physics and Astronomy Research Council of the United Kingdom, the Netherlands Association for Scientific Research, and the National Research Council of Canada.

[4] http://www.iram.fr/IRAMFR/GILDAS

Dust data	wavelength [μm]	beam FWHM [$''$]	rms noise [mJy beam^{-1}]	κ_{dust} [cm^2 g^{-1}]	lowest contour [mJy beam^{-1}]	column density threshold [cm^{-2}]
ATLASGAL/APEX	870	19.2	50	1.42	310	1×10^{22}
MAMBO/IRAM 30 m	1200	10.5	17	0.79	60	2×10^{22}
SCUBA/JCMT	850	14.0	14	1.48	176	1×10^{22}

Table 2. Summary of the different dust data used, and the corresponding properties. The column densities have been calculated under the assumptions given in Sec. 2.6 for 20 K. The last column is the column density corresponding to the lowest emission contour used within *CLUMPFIND*.

The rms of our observations limits the detection of signal, but the N_2H^+ column density also depends on the measured opacity and assumed temperature. As we discuss in Sect. 3.1, we use a constant gas temperature of 20 K. Varying the temperature by up to 5 K, the calculated column densities vary by less than 25%. Taking also the error on the integrated intensity and the partition function into account, we assume the error on the column density to be on the order of 50%. With the given rms toward the edge of the MOPRA data, our theoretical $5\,\sigma$ N_2H^+ detection limit in the optically thin case is given by 1.5×10^{12} cm^{-2} for the velocity resolution of 0.2 km/s. However, since most sources have considerable optical depth, the smallest measured N_2H^+ column density is larger. Their minimal calculated values are given in Table 1. Similarly, for the Nobeyama 45 m data the $5\,\sigma$ detection limit is 2.1×10^{12} cm^{-2}. Since some central regions of e.g. IRDC 18223 have a much lower rms of only 0.05 K instead of 0.12 K, here the lowest calculated values are actually smaller.

The uncertainties on the fit parameters velocity and linewidth are mainly constrained by the signal-to-noise ratio and the line shape. Since even the broadest velocity resolution within our sample of 0.5 km/s resolve the lines, the uncertainties on the linewidth are similar for all data. Spectra with a signal-to-noise better than $7\,\sigma$ and Gaussian shaped line profiles have typical linewidth uncertainties < 5%, while non-Gaussian line profiles and low signal-to-noise ratios may lead to uncertainties of up to 20%. Instead, the recovery of the peak velocity shows an additional slight velocity resolution dependency. Still, both line shape and signal-to-noise ratio dominate, and down to a peak line strength of $3\,\sigma$, the uncertainties on the velocity are below 0.2 km/s.

2.6. Identification of dust peaks

To put the molecular line data in context to its environment we use the dust continuum to obtain gas column densities and masses. For the calculation of column densities from fluxes we use

$$N_{gas} = \frac{RF_\lambda}{B_\lambda(\lambda, T)\mu m_H \kappa \Omega}, \quad (3)$$

with the gas-to-dust mass ratio R = 100, F_λ the flux at the given wavelength, $B_\lambda(\lambda$,T) the blackbody radiation as a function of wavelength and temperature, μ the mean molecular weight of the ISM of 2.8, m_H the mass of a hydrogen atom, and the beam size Ω. Assuming typical beam averaged volume densities in the dense gas of 10^5 cm^{-3} and dust grains with thin ice mantles, we can interpolate the dust mass absorption coefficient from Ossenkopf & Henning (1994) to the desired wavelength. The corresponding dust opacities for the different wavelengths are listed in Table 2.

The gas and dust temperatures should be coupled at densities typical for dense clump ($> 10^5$ cm^{-3}, Goldsmith 2001), and have been measured to be between 15 K and 20 K (Sridharan et al. 2005; Pillai et al. 2006; Peretto & Fuller 2010; Battersby et al. 2011; Wilcock et al. 2011; Vasyunina et al. 2011; Wienen et al. 2012; Wilcock et al. 2012). Since most regions in our survey show already signs of ongoing star formation, we assume a single temperature value of 20 K for all clumps.

With the distance d as additional parameter, the mass can be calculated from the integrated flux in a similar way as given above,

$$M_{gas} = \frac{Rd^2 F_\lambda}{B_\lambda(\lambda, T)\kappa}. \quad (4)$$

To identify emission peaks and their connected fluxes in the dust maps we use CLUMPFIND (Williams et al. 1994). Since we want to compare our results to the dense gas measured by N_2H^+, we select a lowest emission contour corresponding to 1×10^{22} cm^{-2} ($> 6\,\sigma$ for ATLASGAL, $> 12\,\sigma$ for SCUBA), or, in the case of ISOSS J20153, 2×10^{22} cm^{-2} ($> 3\,\sigma$). Additional levels are added in steps of $3\,\sigma$, see Table 2. All clumps for which we mapped the peak position are listed together with their column density and mass in Table 6. For clumps that have common names in the literature, we try to adopt their previous labeling. The clump names and references are given in Table 6 as well.

The uncertainties on both the gas column density and mass are dominated by the dust properties. The flux calibration of the ATLASGAL data is reliable within 15%, and typical peak and clump-integrated fluxes are an order of magnitude larger than the rms of the data. The uncertainties on the dust properties are difficult to assess, but from comparison to other values (e.g. Hildebrand 1983) or using slightly different parameters within the same model (Ossenkopf & Henning 1994) we assume them to be on the order of a factor two. Together with the uncertainties from the dust temperature, we estimate the total uncertainties on the column densities to be a factor of ~ 3. For the gas mass, the uncertainty of the distance of ~ 0.5 kpc introduces an additional error of ~ 50%. Therefore, the total uncertainty of the gas mass we estimate to be on the order of a factor of five.

2.7. Abundance ratio

For positions where not only dust continuum but also N_2H^+ has been detected we calculate abundance ratios. With a resolution of $18''$and $19.2''$, the Nobeyama 45 m data have almost the same resolution as the ATLASGAL 870 μm data. Therefore we calculate the N_2H^+ abundance ratio by plain division, taking the different beam size into account but not smoothing the data. To calculate abundance ratios for sources observed with MOPRA at a resolution of $46''$, we apply a Gaussian smoothing to the dust data to have both at a common resolution. We then calculate the N_2H^+ abundance for the $46''$beam. For the analysis, we only considered dust measurements in the Gaussian smoothed images above $3\,\sigma$.

3. Morphology of the dense gas

In the following section we concentrate on the N_2H^+ observations. First we compare the N_2H^+ to the cold dust distribution as measured by ATLASGAL and put it in context with the PACS 70 μm measurements. Then we describe the velocity and linewidth distribution of the dense gas.

3.1. Comparing integrated N_2H^+ and dust continuum emission

The left panels of Fig. 1 through Fig. 4 display the PACS 70 μm maps with the long-wavelength dust continuum contours on top, the second left panel is the N_2H^+ column density. They clearly show that the N_2H^+ detection and column density agrees in general with the measured dense gas emission, almost independent of the evolutionary state of the clump.

The southern component of IRDC G11.11 appears to be peculiar, see Fig. 2. While for the northern component the molecular gas traced by N_2H^+ agrees quite well with the cold gas traced by thermal dust emission, both dense gas tracers seem to disagree for the southern part. Comparing the brightest peak in the ATLASGAL data to the column density peak of the N_2H^+ emission, we find a positional difference of 37″, which is on the order of the beam size. Since the northern and southern component have been observed independently, a pointing error could explain the offset. However, before and in between the OTF observations we checked the pointing and the offset is considerably larger than the anticipated pointing uncertainty. Therefore, we cannot explain the spatial offset of the southern map well.

For IRDC 18182, the bright north-western component is connected to IRAS 18182-1433 at a velocity of 59.1 km/s (Bronfman et al. 1996) and a distance of 4.5 kpc (Faúndez et al. 2004). Instead, the region of interest is the IRDC in the south-east at a distance of 3.44 kpc with a velocity of 41 km/s (Beuther et al. 2002a; Sridharan et al. 2005).

IRDC 18308 has been selected within this sample for its infrared dark cloud north of the HMPO IRAS 18308-0841. However, at its distance of 4.4 kpc we do not detect the N_2H^+ emission from the IRDC with the velocity resolution of 0.2 km/s. To overcome the sensitivity issue we smoothed the velocity resolution to 0.4 km/s and then can trace the dense gas of the IRDC within IRDC 18308. For IRDC 18306 the situation is similar, we trace the HMPO, but not the IRDC. However, even with a velocity resolution of only 0.4 km/s we cannot detect N_2H^+ from the IRDC. Therefore, we exclude IRDC 18306 from the discussion and show its dense gas properties in the appendix A.2. To get a better picture of the different regions we display in Fig. 1 through Fig. 4 the results from the smoothed maps, where helpful. However, because the coverage for many clumps is sufficient in the higher resolution data, we used the 0.2 km/s data to do our analysis.

The total gas peak column densities over the 19.2″APEX 870 μm beam as given in Table 6 range from 1.4×10^{22} cm^{-2} to 8×10^{23} cm^{-2}, and the median averaged peak column density of clumps that have been mapped is 2.6×10^{22} cm^{-2}. If we consider only clumps for which the peak position has a detected N_2H^+ signal, the median averaged peak column density becomes 3.0×10^{22} cm^{-2}. For the lower limit one needs to keep in mind that we require a minimum column density threshold of 1.0×10^{22} cm^{-2} for a clump to be detected. The upper limit is set by IRDC 18454-mm1 (adopted from W43-mm1, Motte et al. 2003; Beuther et al. 2012), the brightest clump within IRDC 18454 and a well known site of massive star formation. All other clumps with peak column densities larger than 1×10^{23} cm^{-2} (IRDC 18151-1, IRDC 18182-1, and G 28.34-2) host evolved cores and could be warmer than 20 K. However, to calculate the column densities we assume a constant average dense gas temperature of 20 K. While this is appropriate for most IRDCs in this sample with ongoing early star formation (cf. point sources in Ragan et al. 2012a), using a higher temperature would decrease their peak column densities. With the exception of W43-mm1, the upper limit of column densities found within our survey's sources then becomes $\sim1\times10^{23}$ cm^{-2} on scales of the beam size.

3.2. N_2H^+ abundance

In order to study the details of the correlation between the dense gas and the related N_2H^+ column density, Fig. 5 shows the pixel-by-pixel correlation between the N_2H^+ abundance ratio versus the flux ratio between the *Herschel* 160 μm and 250 μm bands. One should keep in mind that, as explained in Sect. 2.7, the abundance ratio refers to different beam sizes, dependent on the telescope that has been used for the observations. The flux ratio of the two PACS bands, or color temperature, can be considered as a proxy of the dust temperature. For higher temperatures, the peak of the SED moves to shorter wavelengths, the 160 μm becomes stronger compared to the 250 μm flux. Therefore, higher temperatures have higher far-IR flux ratios. However, in order to derive proper temperatures, a pixel by pixel SED fitting is required, which will be done in an independent paper (Ragan et al., in prep.). A known issue in the context of *Herschel* data are the unknown background flux levels. Since we only discuss trends within individual regions, we can safely neglect this problem. However, the flux ratios between the different regions are not directly comparable.

To allow a comparison between IRDCs and regions that do not show up in extinction, we marked pixels that lie within regions of high extinction in green. Those regions were selected by visually identifying the 70 μm flux levels under which extinction features are observed. As the 70 μm dark regions have no sharp boundaries, the chosen levels are not unambiguous.

Figure 5 shows no strong overall correlation between the N_2H^+ abundance and the flux ratio. On the one hand, IRDC 18223 is an example where there seems to be a correlation between the temperature and the N_2H^+ abundance. The highest abundance ratios are found at far-IR flux ratios of the bulge of the pixel distribution, while toward higher temperatures the abundance seems to decrease systematically. On the other hand, in G11.11 the N_2H^+ abundance varies over two orders of magnitude, but shows no correlation with the far-IR flux ratio. For example in G11.11 and G28.34, there seems to be a trend that the N_2H^+ abundances become even larger toward the edges of our N_2H^+ mapping. However, in these regions we are limited by the sensitivity of our dust measurements.

Marked by an 'X' in Fig. 5 are the pixels containing PACS point sources. In addition, we distinguish between sources that have only been detected at 70 μm and longwards, MIPS-dark sources, and PACS sources that have a 24 μm counter part, MIPS-bright sources. If the 24 μm image is saturated at the given position, sources are considered as MIPS-bright as well. From the figure it can be seen that most embedded PACS sources have N_2H^+ abundance ratios below 1×10^{-9}. However, there seems to be no correlation between the dust temperature on scales of the beam size and the presence of embedded PACS point-sources.

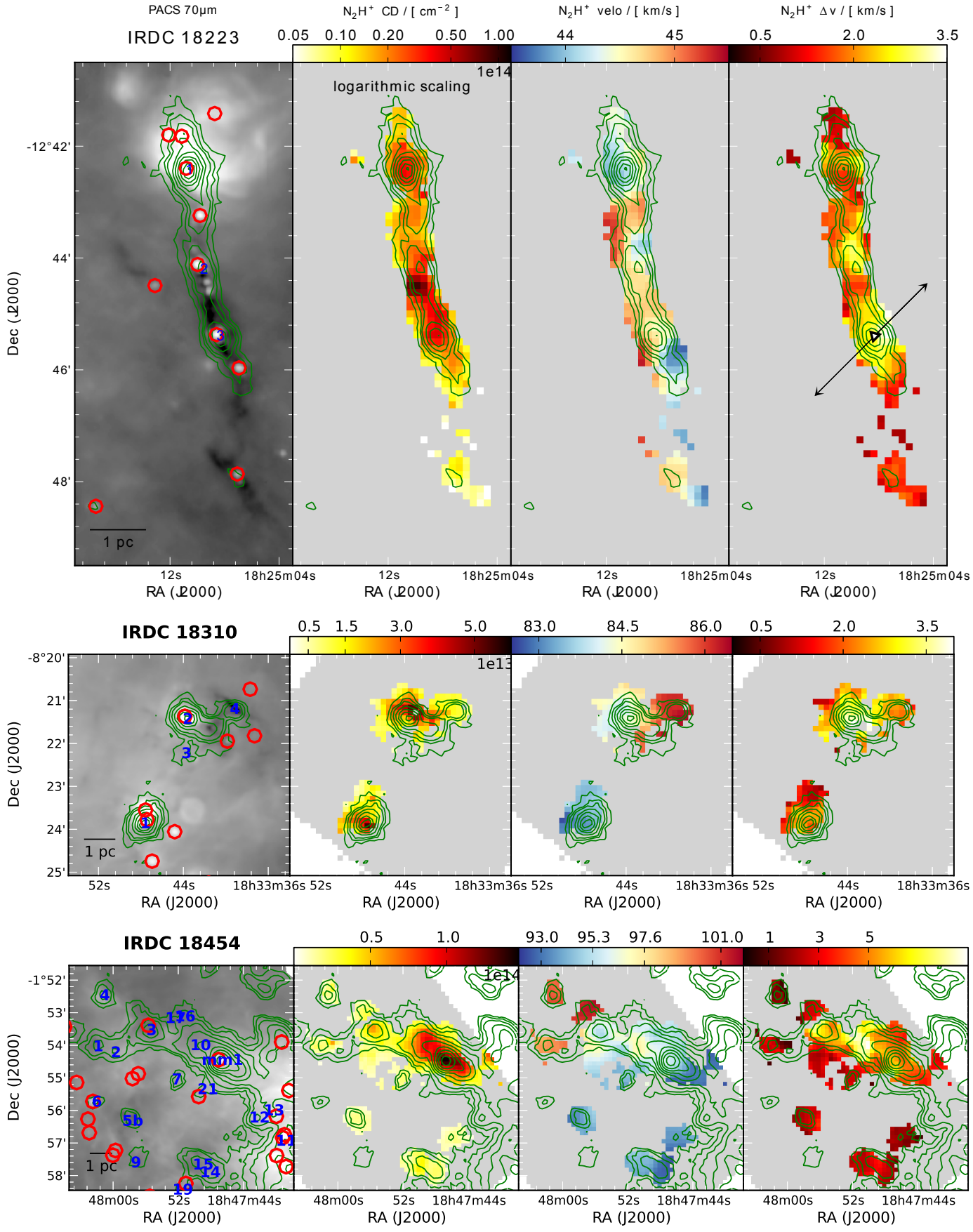

Fig. 1. Parameter maps of the regions IRDC 18223, IRDC 18310, and IRDC 18454 mapped with the Nobeyama 45 m telescope, at top, middle, and bottom panel, respectively. The left panel of each row are the PACS 70 μm maps with the PACS point sources detected by Ragan et al. (2012a) indicated by red circles, the blue numbers refer to the sub-mm continuum peaks as given in Table 6. The second panel displays the N_2H^+ column density derived from fitting the full N_2H^+ hyperfine structure. The third and fourth panels show the corresponding velocity and linewidth (FWHM) of each fit. For IRDC 18223, and IRDC 18310 the contours from ATLASGAL 870 μm are plotted with the lowest level representing 0.31 Jy, and continue in steps of 0.3 Jy. The contour levels for IRDC 18454 are logarithmically spaced, with 10 levels between 0.31 Jy and 31 Jy. The column density scale of IRDC 18223 is logarithmic. The arrow in the fourth panel of IRDC 18223 is taken from Fig. 4 of Fallscheer et al. (2009), indicating the outflow direction.

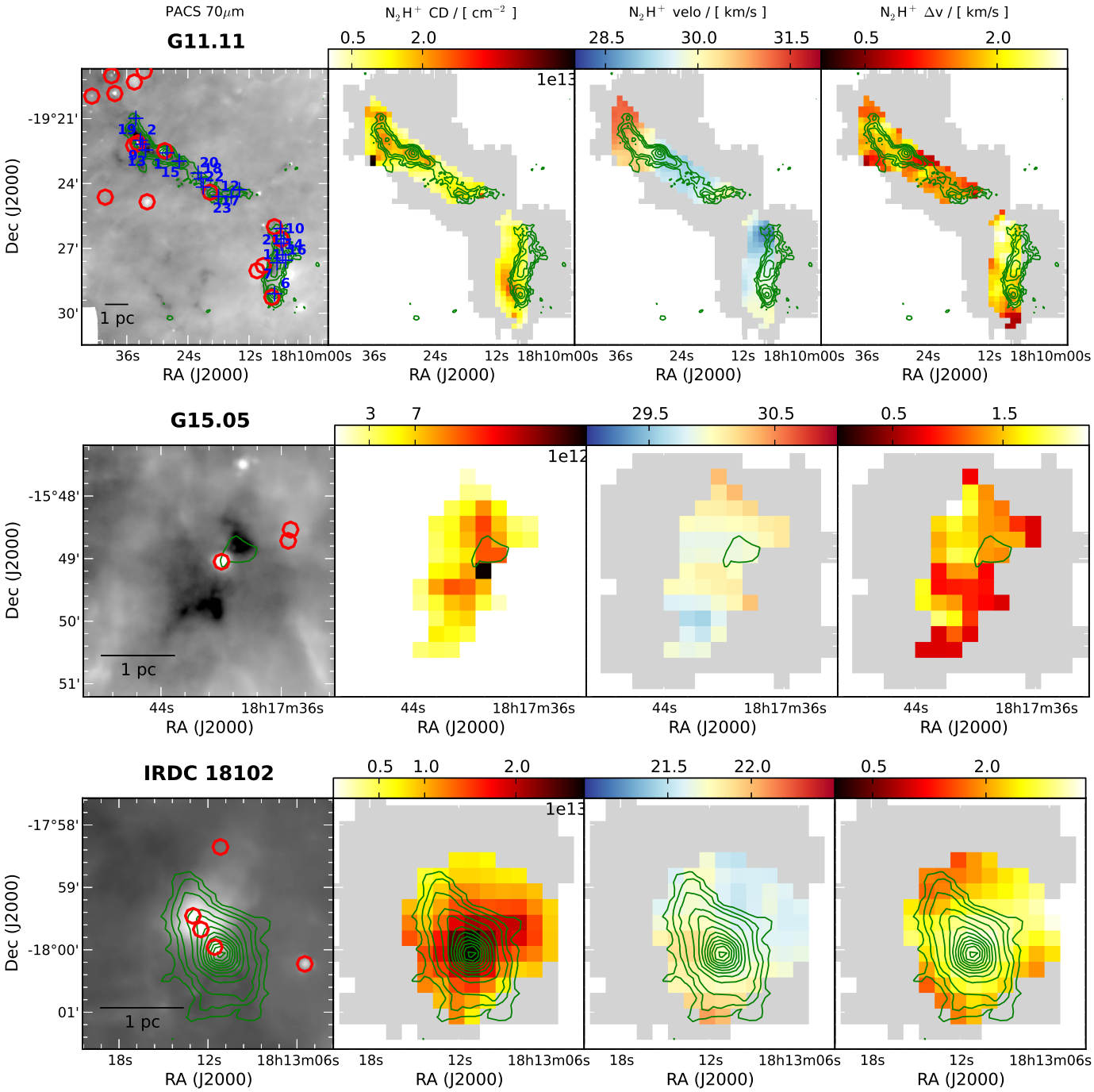

Fig. 2. Parameter maps of the regions G11.11, G15.05, and IRDC 18102, mapped with the MOPRA telescope. The left panel of each row are the PACS 70 μm maps with the PACS point sources detected by Ragan et al. (2012a) indicated by red circles, the blue numbers refer to the sub-mm continuum peaks as given in Table 6. The second panel displays the N_2H^+ column density derived from fitting the full N_2H^+ hyperfine structure. The third and fourth panels show the corresponding velocity and linewidth (FWHM) of each fit. The green contours are from ATLASGAL 870 μm at 0.31 Jy, 0.46 Jy, and 0.61 Jy, continuing in steps of 0.3 Jy. The velocity resolution in the G15.05 map is smoothed to 0.4 km/s to improve the signal to noise and increase the number of detected N_2H^+ positions.

3.3. The large scale velocity structure of clumps and filaments

The velocity structure of the N_2H^+ gas is shown in the third panel (second from right) of Fig. 1 to Fig. 4. As explained in Sect. 2.5, we fit a single N_2H^+ hyperfine structure to every pixel and display the resulting peak velocity.

The south-eastern region in the map of IRDC 18182 is the IRDC in the EPoS sample. It already had been known that IRAS 18182-1433, originally targeted by Beuther et al. (2002a), and the IRDC have different velocities and therefore are spatially distinct. All other sources mapped show velocity variations of only a few km/s and are therefore coherent structures.

The source with the largest spread in velocity is IRDC 18454 / W43. The mapped regions in the west, beyond W43-mm1 toward W43-main (which has not been mapped), have the lowest velocities at below 93 km/s, then there is a ve-

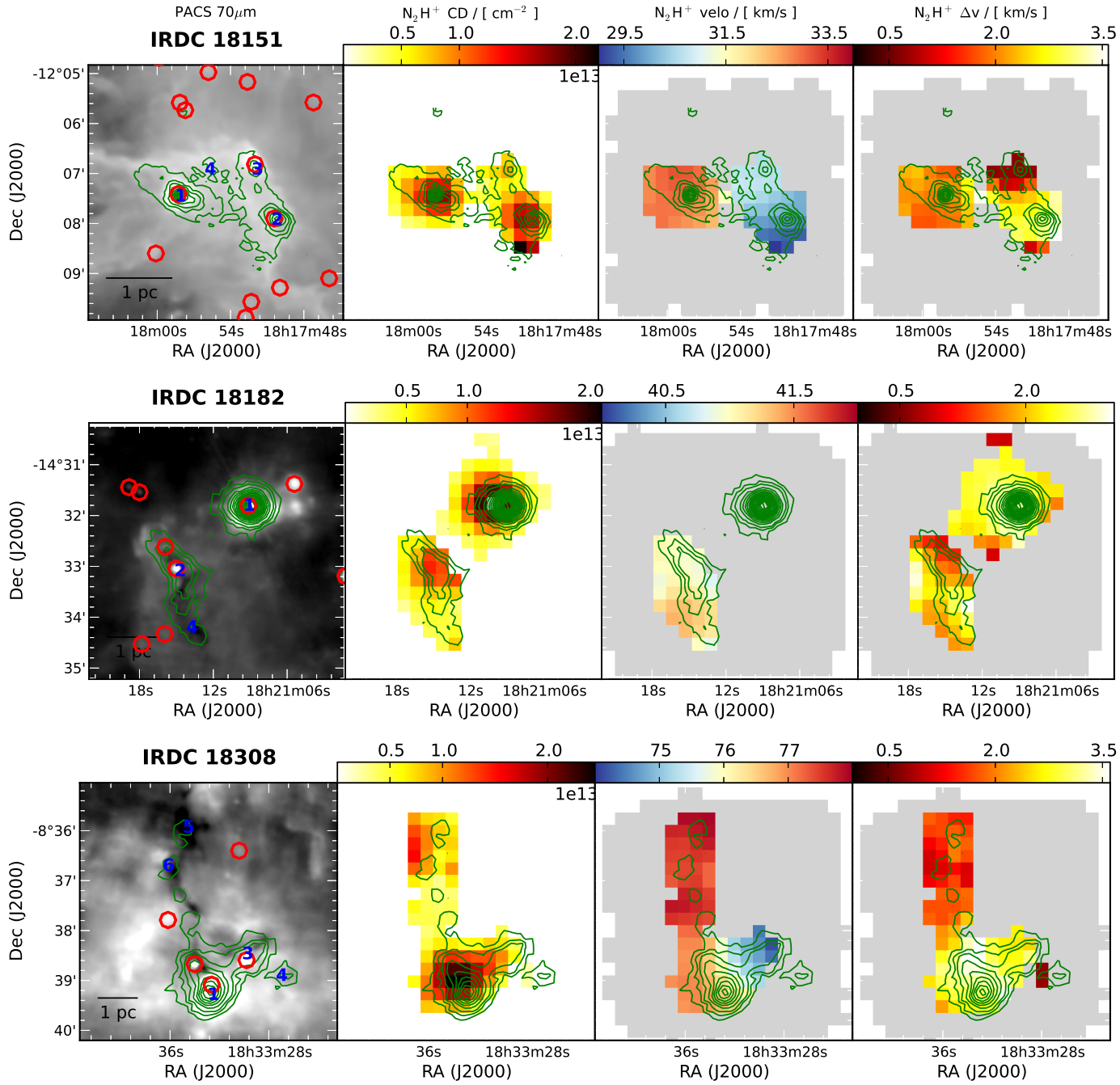

Fig. 3. Parameter maps of the regions IRDC 18151, IRDC 18182, and IRDC 18308, each mapped with the MOPRA telescope. The left panel of each row are the PACS 70 μm maps with the PACS point sources detected by Ragan et al. (2012a) indicated by red circles, the blue numbers refer to the sub-mm continuum peaks as given in Table 6. The second panel displays the N_2H^+ column density derived from fitting the full N_2H^+ hyperfine structure. The third and fourth panels show the corresponding velocity and linewidth (FWHM) of each fit. The green contours are from ATLASGAL 870 μm at 0.31 Jy, 0.46 Jy, and 0.61 Jy, continuing in steps of 0.3 Jy. For IRDC 18151 the contours are MAMBO 1.2 mm observations, starting at 60 mJy in steps of 60 mJy. In all three maps the velocity resolution is smoothed to 0.4 km/s.

locity gradient across W43-MM1 ending east at 97.4 km/s, and in the very south there are two clumps at 100 km/s. However, the velocity map has been derived fitting a single N_2H^+ hyperfine structure to each spectrum. Beuther & Sridharan (2007) and Beuther et al. (2012) have shown that, at least at high spectral and spatial resolution, clump IRDC 18454-1 has two velocity components seperated by about 2 km/s. Trying to fit each clump peak position with two N_2H^+ hyperfine structures, we find that for six continuum peaks, the N_2H^+ spectrum is better fitted by two independent components. For simplicity, we do not include the additional velocity component found towards IRDC 18454 at ~ 50 km/s (Nguyen Luong et al. 2011).

While a more detailed description of the double line fits are presented in Sect. 3.4, we here want to note that the mapped line velocity is representing either a single component if one is much brighter than the other, or an average velocity of both. Therefore, the uncertainties for IRDC 18454 are significantly larger than for the other regions. Nevertheless, the large-scale velocity gradient is no artifact but is evident in the individual spectra.

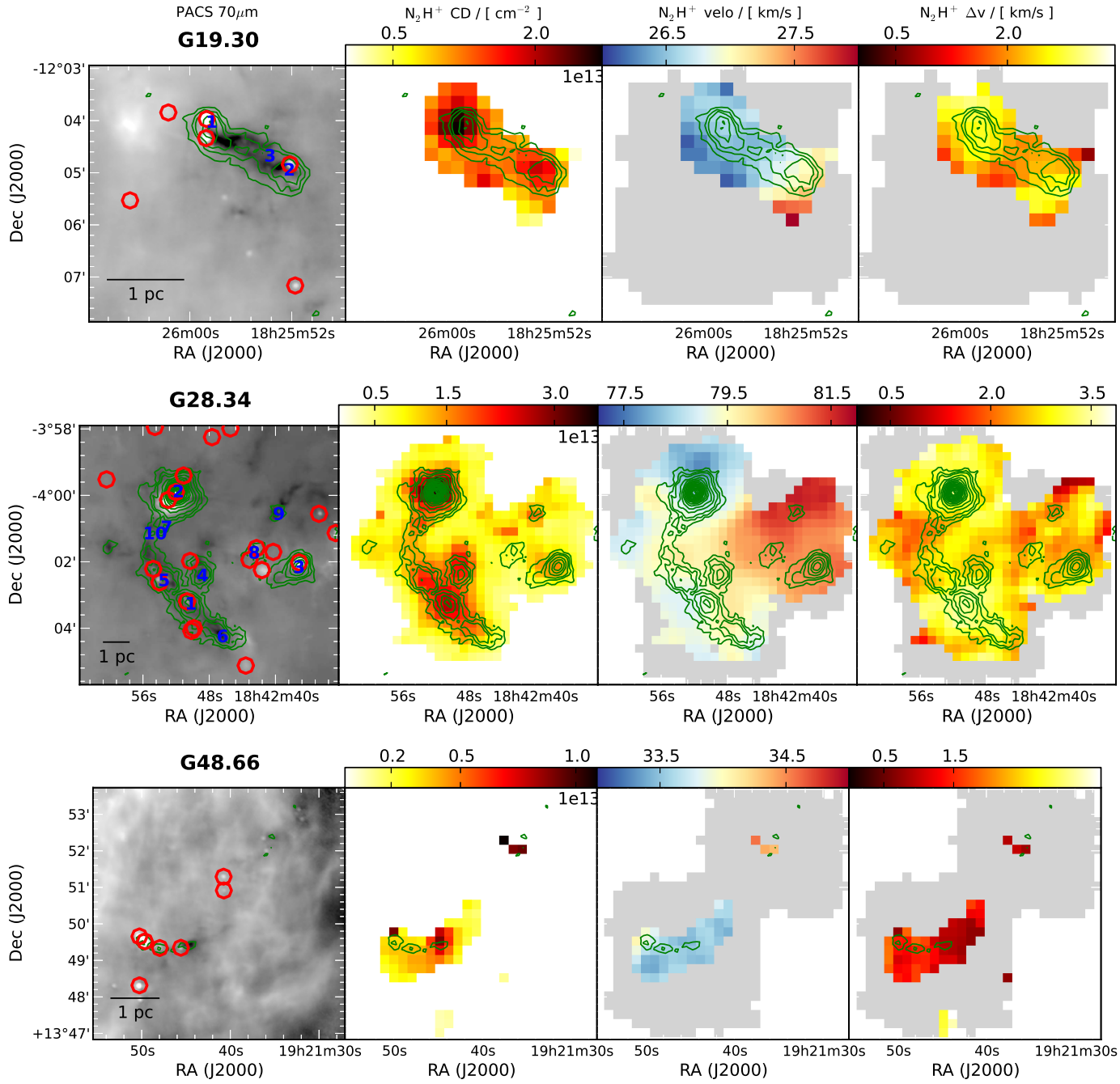

Fig. 4. Parameter maps of the regions G19.30, G28.34, and G48.66, each mapped with the MOPRA telescope. The left panel of each row are the PACS 70 μm maps with the PACS point sources detected by Ragan et al. (2012a) indicated by red circles, the blue numbers refer to the sub-mm continuum peaks as given in Table 6. The second panel displays the N_2H^+ column density derived from fitting the full N_2H^+ hyperfine structure. The third and fourth panels show the corresponding velocity and linewidth (FWHM) of each fit. The green contours are from ATLASGAL 870 μm at 0.31 Jy, 0.46 Jy, and 0.61 Jy, continuing in steps of 0.3 Jy. In all three maps the velocity resolution is smoothed to 0.4 km/s.

Studying the velocity maps in Fig. 1 through Fig. 4 in more detail, we find two different patterns of velocity structure. On the one hand we find independent clumps that lie within the same region and may now or in the future interact, but are currently separate entities in velocity. A good example is IRDC 18151 plotted in Fig. 3. Using 870 μm as dense gas tracer we resolve two clump complexes separated by $\sim$ 1 pc. Across each clump there are only little velocity variations, but the east and west complex are separated in velocity space by 3.3 km/s. Velocity differences on the order of a few km/s between clumps within the same structure are common and we consider such clumps as spatially connected.

On the other hand, we find smooth velocity gradients across larger structures. Clumps, which may be at different velocities, have connecting dense material with a continuous velocity transition in between. To exclude overlapping, but independent clumps for which either the spatial resolution or our mapping technique mimic a smooth transition we searched for double-peaked velocities and a broadening of the line width in such transition zones.

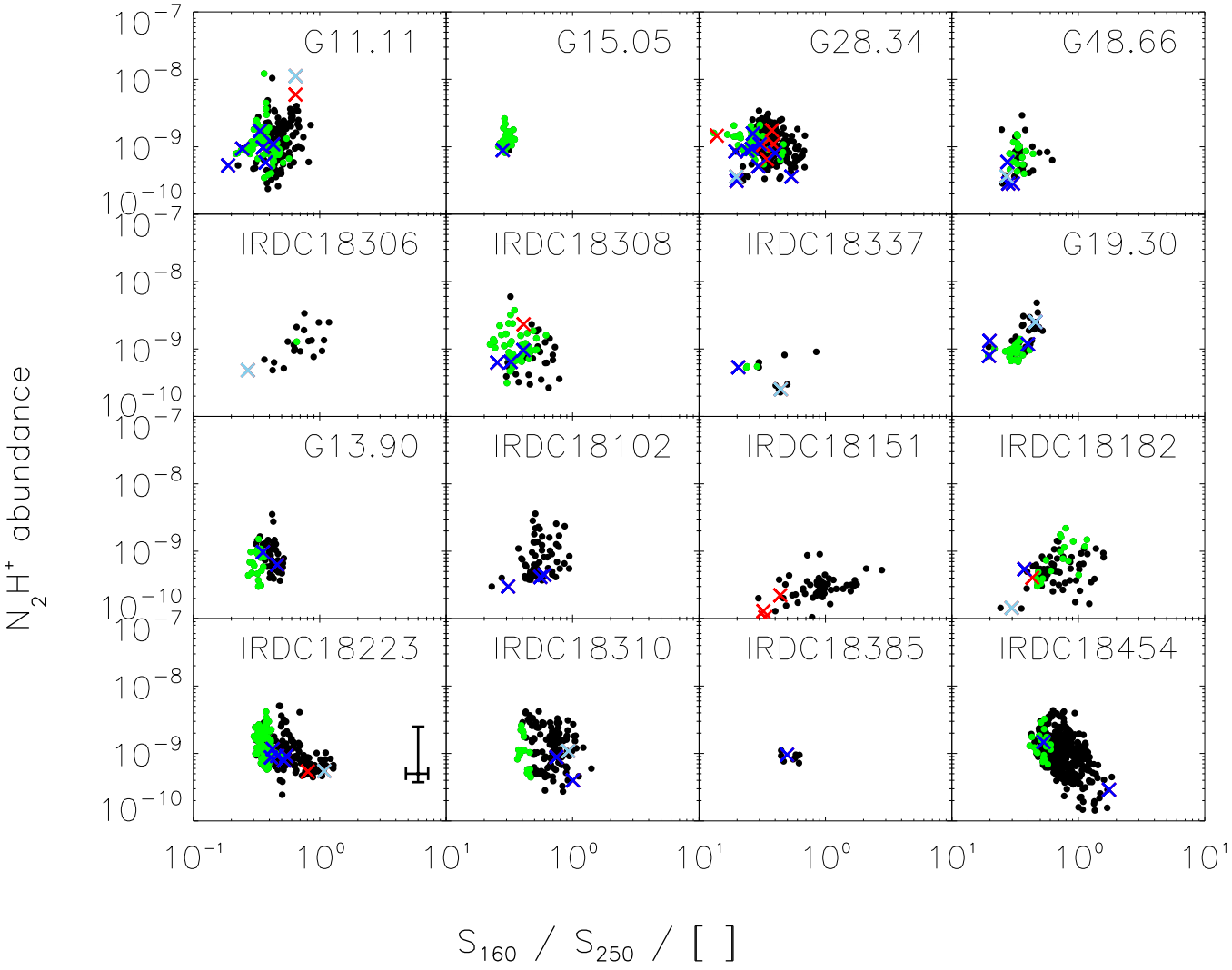

Fig. 5. Plotted is the N_2H^+ abundance ratio over the color index between 160 μm and 250 μm. Marked by green dots are pixels that lie within IRDCs. Overplotted with red Xs are all PACS sources that have been mapped. Blue crosses also have a 24 μm detection, while the light blue dots represent source that are saturated at 24 μm. The uncertainties given for IRDC 18223 are representative for all regions.

The velocity maps of G15.05, IRDC 18102, IRDC 18151, IRDC 18182, and G48.66, Fig. 1, Fig. 2, Fig. 3, and Fig. 4, immediately reveal that those complexes have no velocity gradients in the gas above our detection limits given in Table 7 and therefore are of the first type. A summary of the clump classification is given in Table 7.

For IRDC 18310, shown in Fig. 1, the velocity map shows that the IRAS source in the south has a velocity of 83.2 km/s (see also Table 6), while the northern complex has larger velocities. Nevertheless, the velocity spread suggests an association between both clumps. In addition, the northern component itself has different velocities toward the east and south, with 86.1 km/s and 84.3 km/s. In between there is a short transition zone with an spatially associated increase in the linewidth (see very right panel of Fig. 1). The increase in linewidth suggests that there is indeed an overlap of two independent velocity components, rather than a large scale velocity transition. Using the unsmoothed Nobeyama image at an velocity resolution of 0.2 km/s, the spectra suggest two independent components. Therefore, IRDC 18310 consists of three clumps, each showing no resolved velocity structure.

IRDC 18151, shown in Fig. 3, consists of two clumps at different velocities. While the velocities of the western clump agree within 0.5 km/s, the eastern clump has a velocity gradient from the south-east to the north-west with a change in velocity of more than 1 km/s. However, at the velocity resolution of 0.2 km/s we do not detect the lower column density transition region and cannot exclude a smooth transition across both clumps. To overcome the sensitivity issue we smooth the N_2H^+ data to a resolution of 0.4 km/s. Still, only a single pixel with a good enough signal to noise ratio connects both dense gas clumps. As we will discuss in Sect. 4.4, the found pattern does not suggest a smooth transition.

For IRDC 18454, IRDC 18308, G11.11, G19.30, and G28.34 we find smooth velocity gradients. One of the largest smooth velocity gradients of the sample is found toward the southern part of IRDC 18308, across the HMPO. Although there is an increase in the linewidth map, even in the unsmoothed higher resolution data we cannot find two independent components. Over 3.2 pc the velocity changes by 2.4 km/s, resulting in a velocity gradient of 0.8 km/s /pc. The change in velocity is parallel to the elongation of the ATLASGAL 870 μm emission.

Table 7. Selected clump properties.

Source	Velocity gradient	Double component	Increase in Δv towards peak	Decrease in Δv towards peak	Outflow dominated Δv	Flow along filament
IRDC 18223	✓[1]		18223-2	18223-1	18223-1[3]	?
				18223-3	18223-3	
IRDC 18310	✗			18310-4		
IRDC 18454	✓	✓				?
IRDC 18102	✗		18102		18102	
IRDC 18151	✗		18151-2	18151-1	18151-2[3]	
IRDC 18182	✗		18182-1	18182-2		
IRDC 18308	✓			18308-1		✓
IRDC 19.30	✓		G19.30-1	G19.30-2	G19.30-1[3]	✓
					G19.30-2[3]	
IRDC 11.11	✓	✓		G11.11-1	G11.11-1[2]	✓
				G11.11-2		
IRDC 15.05	✗				G15.05[3]	
IRDC 28.34	✓		G28.34-1	G28.34-10	?	
			G28.34-2			
IRDC 48.66	✗				G48.66[3]	

The columns are as follows: full region name; flag indicating whether we find a smooth velocity gradient along the region; flag indicating the presence of resolved independent velocity components along a line of sight; two columns for clumps for which we find a clear increase in linewidth towards the center and towards the edge clumps, respectively; flag indicating that the velocity profile is consistent with flows along the filament. Notes: (1) For 18223 we find several velocity gradients, both along and perpendicular to the filament. (2) The angle between the outflow and the linewidth broadening does not match exactly. (3) Indirect evidence for outflow (mainly from SiO), but the direction of the outflow is unknown.

The velocity gradient in the northern part of G11.11 is similarly clear as it is for IRDC 18308 and is parallel to the extinction of G11.11. While the very southern tip of the northern filament is at a slightly different velocity, up north it has an almost constant velocity up to the point G11.11-1 and then shows a strong but smooth gradient beyond.

As mentioned before, if considering the length and change in velocity only, the samples largest velocity gradient is found for IRDC 18454. Over a length of 8.4 pc the gradient is 0.9 km/s /pc. However, in between the two endpoints the velocity is not increasing monotonically.

IRDC 18223 shows significant changes in the velocity field, but is not listed among the clumps with smooth velocity gradients. The changes of the velocity are on 0.5 pc - 1 pc scales and show no clear pattern. Nevertheless, at the given velocity resolution of 0.5 km/s we do not find overlapping independent N_2H^+ components. Therefore, all the gas on the scales we trace seems to be connected. It is worth noting that the two southern clumps, IRDC 18223-2 and IRDC 18223-3, have a gradient along the short axis of the filament, which might be interpreted as rotation. Velocities in the east are larger than the velocities in the west. In contrast, although less well mapped, the IRAS source in the north, IRDC 18223-1, has a velocity gradient along the short filament axis, too, but in opposite direction; velocities in the west are larger than in east.

For G13.90, IRDC 18385, IRDC 18306, and IRDC 18337 we lack the sensitivity to draw a conclusion. While IRDC 18385, and IRDC 18306 are not reasonable mapped at all, for G13.90 and IRDC 18337 we map the main emission structures, but with the given sensitivity we do not trace the gas in between the dense clumps. In both sources, the detected clumps have differing velocities, with a gradient accross the clumps in IRDC 18337. However, since we do not trace the gas in between the dense clumps, we cannot assess whether the velocity transitions are smooth, or the clumps have no connection in velocity space.

3.4. The N_2H^+ linewidth in context of young PACS sources and column density peaks

The right panel of Fig. 1 to Fig. 4 show the fitted linewidth (FWHM) for the mapped regions. The distribution of the linewidth is very different for each region and density peak. While it increases toward some of the sub-mm peaks (e.g. IRDC 18102, IRDC 18182-1), for others the peak of the linewidth is on the edge of the sub-mm clumps (e.g. IRDC 18223-1, IRDC 18223-3, G19.30). The IRDCs for which we detect N_2H^+ and that have no embedded/detected PACS source often have a smaller linewidth than other clumps of the same region with embedded protostars.

A brief description of the linewidth distribution of each region is given in the Appendix A. In the following we discuss a few interesting/notable examples.

While the linewidth in IRDC 18223 increases toward IRDC 18223-2 significantly, the linewidth toward IRDC 18223-1, a well studied HMPO (Sakai et al. 2010), and IRDC 18223-3, an object known to drive a powerful outflow (Beuther & Sridharan 2007; Fallscheer et al. 2009), increases toward the edges of the dust continuum. Compared to other regions of IRDC 18223, the linewidth at IRDC 18223-3 is elevated, but it broadens further toward the north-west. This aligns very well with the outflow found by Fallscheer et al. (2009) and can be explained by it (for the outflow direction see the first row of Fig. 1, right panel). IRDC 18223-1 was originally identified as IRAS 18223-1243 and is bright at IR wavelengths (down to K band). However, typical tracers of ongoing high-mass star formation such as cm emission, water and methanol masers, or SiO tracing shocks are not detected (Sridharan et al. 2002; Sakai et al. 2010). Only the CO line wings found by Sridharan et al. (2002) are indicative of outflows, which could explain the bipolar broadening of the N_2H^+ linewidth well. Nevertheless, despite its prominence at IR wavelengths and with the luminosity of the PACS point source at its peak of 2000 $L_\odot$ (point source 8 in Ragan et al. 2012a), the linewidths at the continuum peak are not exceptional within this

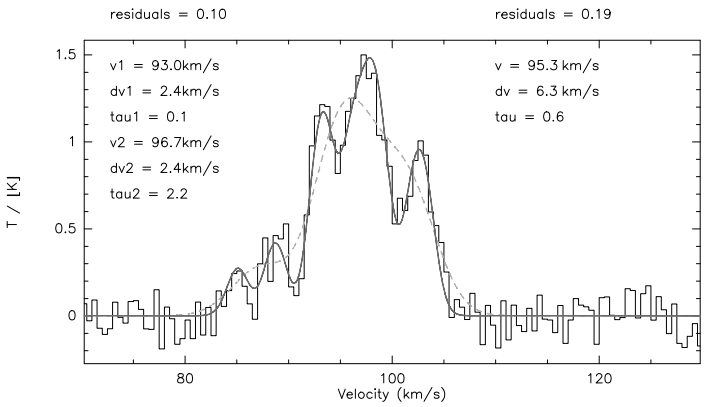

Fig. 6. Spectra of IRDC 18454-4 Beuther & Sridharan (2007); Beuther et al. (2012). While the dashed line shows the single component fit with the fitting parameters to the right, the solid line is the two component fit with its fitting parameters to the left. The given residuals are the results of the *minimize* task in *CLASS*.

region. In contrast, although IRDC 18223-2 is detected at near IR wavelengths as well and the PACS point source at its center has a luminosity of only 200 $L_\odot$, the linewidth is 2.5 kms/s compared to 1.9 km/s for IRDC 18223-1. Since Beuther & Sridharan (2007) find no SiO toward IRDC 18223-1/2 we exclude a strong outflow, and the reason for the line broadening is not clear at all. However, IRDC 18223-2 has not been addressed in such great detail and we cannot entirely exclude an outflow.

We exclude IRDC 18454 from the analysis of the linewidth since, as already mentioned in Sect. 3.3, we find multiple velocity components toward several positions. Figure 6 displays an example of an N_2H^+ spectrum that compares a single component fit to a double component fit. Comparing the residuals of the two different fits as calculated by *CLASS*, for the six clumps in which we find two independent components the residuals are on average reduced by 30%. As for all two component fits, the linewidth decreases compared to a single component fit. However, the linewidths are then on average still larger than for the other clumps listed in Table 6.

Similar double velocity component fits toward the peaks are otherwise only possible in G11.11. Here, eight of the clumps are fit better by two independent N_2H^+ components. However, different from IRDC 18454 the linewidth of the two components become on average smaller than the linewidth of other clumps in the sample. In addition, the improvement of the residuals is only 20%. Therefore it is unclear whether two independent components are present or the fit is simply improved because of the larger number of free parameters. However, a systematic study of the multiple components is beyond the scope of this paper.

For G13.90, IRDC 18385, IRDC 18306, and IRDC 18337 the mapped areas are not sufficient to draw conclusions.

Similar to Fig. 5, Fig. 7 shows the relation between the linewidth (FWHM) of N_2H^+ and the color index. Since the color index is a proxy of the temperature, a correlation between both quantities could have been expected. However, we do not see any correlation. Figure 8 plots the N_2H^+ linewidth versus the H_2 column density, but we find no correlation.

In the context of the linewidth and dust mass, the virial analysis can be used to understand whether structures are gravitationally bound or are transient structures. Following MacLaren et al. (1988), we calculate the virial mass of our clumps via $M_{vir} = k\,R\,\Delta v^2$. For the clump radius R we use the effective radius calculated by CLUMPFIND. The geometrical parameter k depends on the density distribution, with k = 190 for $\rho \sim r^{-1}$, and

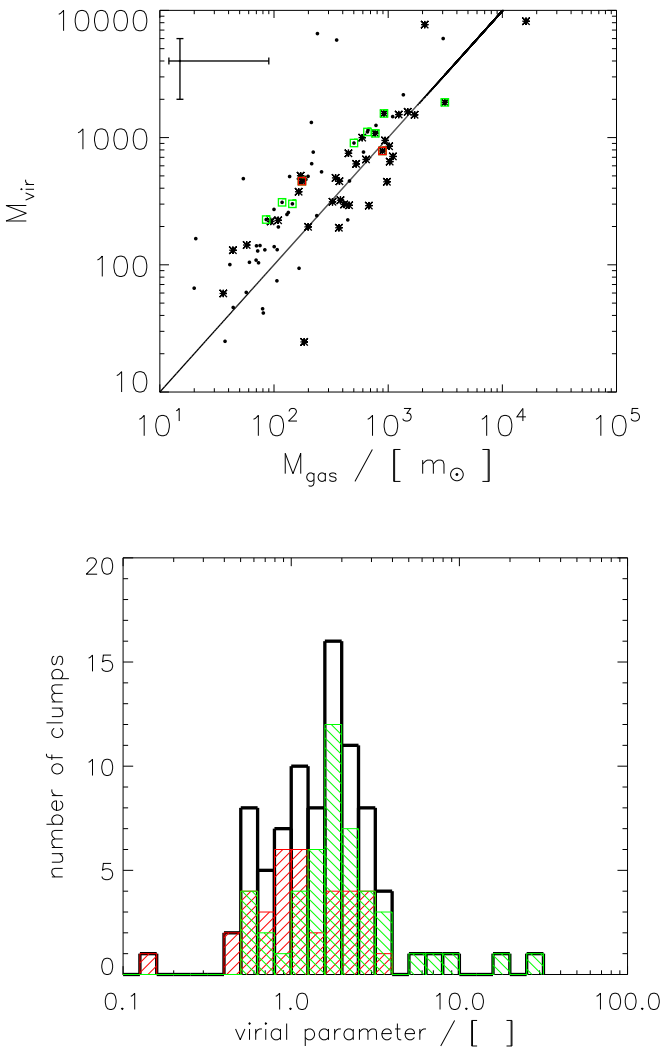

Fig. 9. Top panel: Plot of the virial mass derived from the N_2H^+ linewidth over the gas mass. The virial mass assumes a geometrical parameter of k=158, which is intermediate between k=126 for $1/\rho^2$ and k=190 for $1/\rho$. While the black dots indicate clumps without a PACS point source inside, the asterisks represent clumps with a PACS point source. Marked by green and red squares are the clumps of G28.34, with green boxes representing clumps in global infall, and red boxes representing clumps with signatures of outwards moving gas (for details see Tackenberg et al., submitted). The solid line indicates unity. Lower panel: Histogram of the virial parameter α. While the black histogram represents the full sample, the red and green histogram is the subset of clumps with and without PACS point source, respectively.

k = 126 for $\rho \sim r^{-2}$. Beuther et al. (2002a), Hatchell & van der Tak (2003), and Peretto et al. (2006) find typical density distributions in sites of massive star formation of $\rho \propto r^{\alpha}$ with $\alpha \sim$ -1.6, in between both parameters. While we list the virial mass for both parameters in Table 6, we use the intermediate value of k = 158 in Fig. 9.

The α parameter as defined in Bertoldi & McKee (1992) is the ratio of the internal kinetic energy and the gravitational energy. However, their virial parameter as defined in Eqn. 2.8a of Bertoldi & McKee (1992) ($\alpha = \frac{5\sigma^2 R}{GM}$) without further geometrical parameter resembles a spherical distribution of constant density. Due to the geometrical correction factor we apply to the

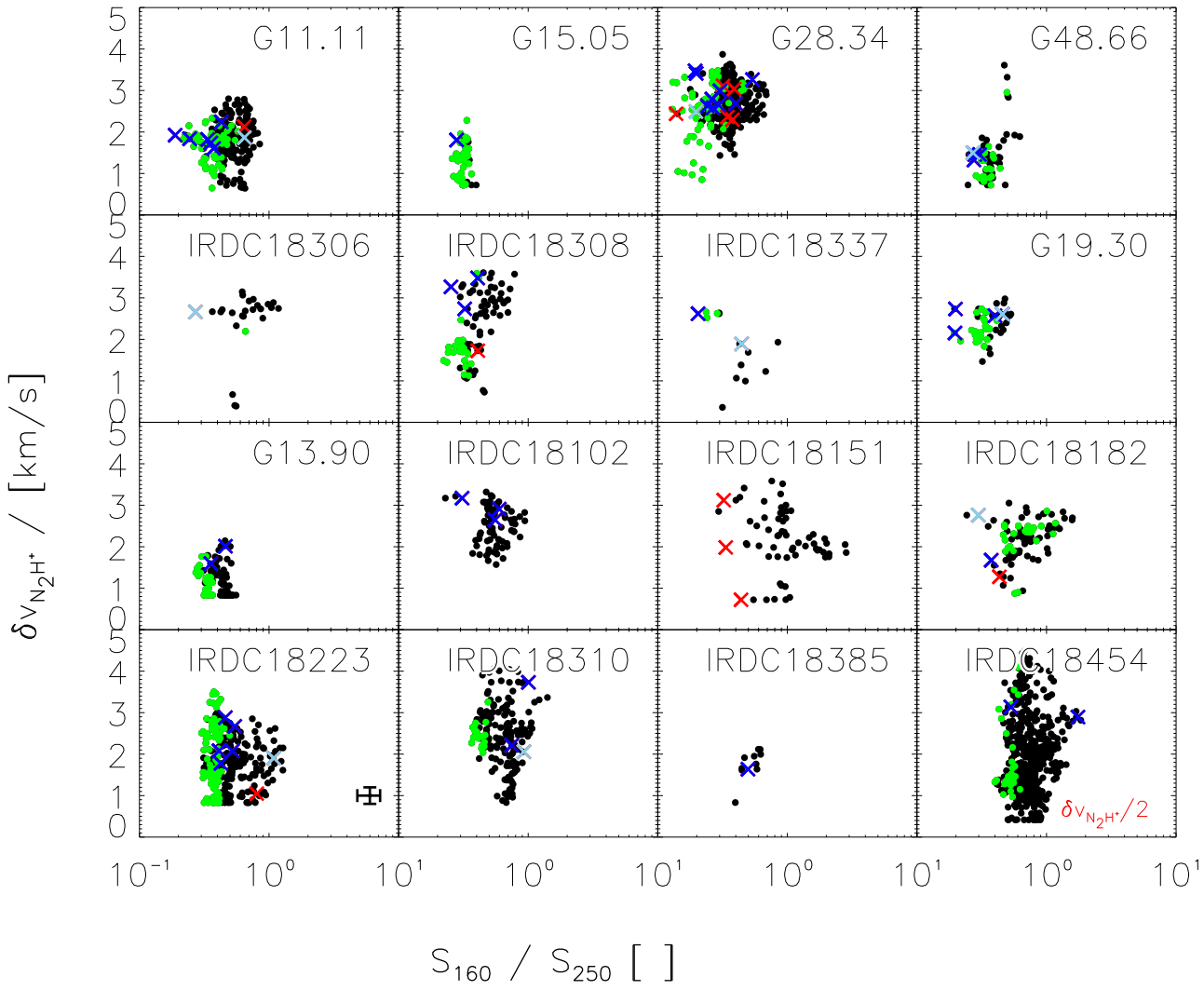

Fig. 7. Plot of the N_2H^+ linewidth versus the color index for the 160 μm over the 250 μm band. Marked by green dots are pixels that lie within IRDCs. Overplotted with red Xs are all PACS sources that have been mapped. Blue dots also have a 24 μm detection, while the pale blue dots represent source that are saturated at 24 μm. The uncertainties given for IRDC 18223 are representative for all regions. For IRDC 18454 the linewidths have been multiplied by a factor of 0.5 in order to fit the data points into the plotting range.

mass calculations, the presented virial parameters are smaller by a factor of 1.32. A histogram of the virial parameter is plotted in Fig. 9.

If we assume the error on our linewidth to be less than 15%, the uncertainties of the calculated virial mass are mainly determined by the geometrical parameter k. The actual error on the given virial masses is significantly larger since the calculation neglects all physical effects but gravity and thermal motions (kinetic energy). However, for the conceptual quantity we can neglect these effects and estimate the error to be ~ 50%.

4. Discussion of N_2H^+ dense gas properties

In the following, we will discuss the kinematic properties of sources we mapped in N_2H^+, as described above.

4.1. Dense clumps and cores

The clump masses in the range of several tens of $M_\odot$ to a few thousands of $M_\odot$ show that most regions have the potential to form massive stars in the future, or show signs of ongoing high-mass star formation. One should keep in mind that the listed peak column densities are averaged over the beam. As it has been shown by Vasyunina et al. (2009) assuming an artifical r^{-1} density profile, true peak column densities are larger by a factor of 20 to 40. This is in agreement with interferometric observations of clumps within our sample (Beuther et al. 2005, 2006; Fallscheer et al. 2011). Therefore, all peak column densities become larger than 3×10^{23} cm^{-2}, or 1 g/cm^2. This reinforces the view that the mapped clumps are capable of forming massive stars. The high column densities are also in agreement with the detection of N_2H^+ as high density gas tracer.

4.2. Abundance ratios

In order to understand why the abundance of N_2H^+ is expected to vary with embedded sources or temperature, one needs to understand the formation mechanism. The formation of N_2H^+ works via H_3^+ which also builds the basis for the formation of HCO^+ from CO. Due to the high abundance of CO in cold dense

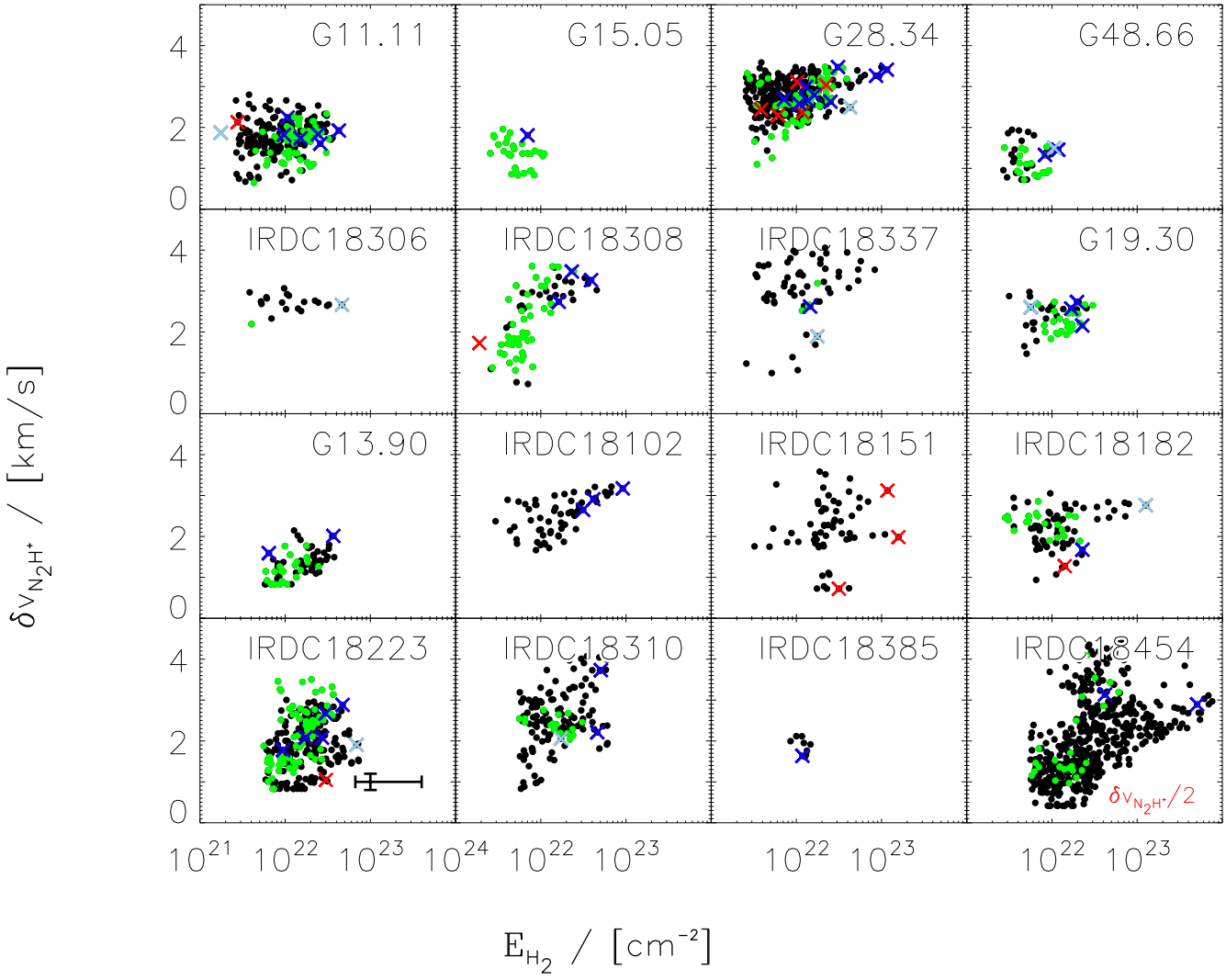

Fig. 8. Plot of the N_2H^+ linewidth versus the dust column density. Marked by green dots are pixels that lie within IRDCs. Overplotted with red Xs are all PACS sources that have been mapped. Blue dots also have a 24 μm detection, while the pale blue dots represent source that are saturated at 24 μm. The uncertainties given for IRDC 18223 are representative for all regions. For IRDC 18454 the linewidths have been multiplied by a factor of 0.5 in order to fit the data points into the plotting range.

clouds, the production of HCO^+ is initially dominant and consumes all H_3^+. However, if during cloud contraction the temperatures become cold enough for CO to freeze out, N_2H^+ can be produced more efficiently and eventually becomes more abundant than HCO^+. The situation changes again when CO becomes released from the grains either due to heating or due to shocks. The CO destroys the N_2H^+ and forms HCO^+ instead, making HCO^+ more abundant again. (For a more detailed discussion see Jørgensen et al. 2004.)

In summary, the early, (more diffuse) cloud phase is dominated by HCO^+, while the quiet dense clumps should be dominated by N_2H^+. With the onset of star formation, HCO^+ is becoming dominant again.

The EPoS sample mainly has been selected to cover regions of ongoing, but early star formation. For this N_2H^+ line survey, we selected regions covering all evolutionary stages. Many of them have both infrared quiet regions at the wavelengths range covered previous to *Herschel* as well as well known and luminous IRAS sources. Together with the *Herschel* data, hardly any region of high column density is genuine infrared dark.

As a result of both the N_2H^+ evolution and the broad range of evolutionary stages covered, we expect a large range of N_2H^+ abundance ratios. As it has been discussed in Sect. 3.2, Fig. 5 shows the correlation between the N_2H^+ abundance and the 160 μm to 250 μm flux ratio as a proxy of the temperature. For all regions, the bulk of all pixels has N_2H^+ abundances ratios of 1×10^{-9}. That is in good agreement with earlier studies of high-mass star-forming regions (Vasyunina et al. 2011, and references therein). At the same time several regions (e.g. G11.11, G28.34, IRDC 18454) show abundance variations of two orders of magnitude. While this is a result of the various evolutionary stages within each region, it is worth noting that it seems not to be correlated to the flux ratio of 160 μm over 250 μm.

In order to correlate some areas with an evolutionary stage, in Fig. 5 we differentiate regions that show up in extinction at 70 μm by green dots. As Fig. 5 shows, these regions are among the coldest within each region. Nevertheless, high N_2H^+ abundances are found not only in IRDCs or cold regions. In contrast to IRDC pixels which mark the earliest and coldest evolutionary stages, the PACS only sources mark regions in which star for-

mation is about to start (red), and the MIPS bright PACS sources indicate ongoing star formation (blue). All pixels connected to a PACS source have low N_2H^+ abundances. Whether this is due to an increase in temperature or probably because of shocks is unclear.

It has been shown in Ragan et al. (2012a) that sources with detected 24 μm counterpart are on average warmer, more luminous, and more massive and therefore a 24 μm counterpart is indicative of a more evolved source. Nevertheless, the PACS core properties in Ragan et al. (2012a) show a large overlap between MIPS bright and dark sources. Therefore, one cannot draw a clear conclusion on the evolutionary stage (temperature, luminosity, or mass) based on a 24 μm detection alone. This easily explains exceptions as e.g. in G11.11.

4.3. Signatures of overlapping dense cores within clumps

As we describe in Sect. 3.3, we find two independent velocity components toward six of the IRDC 18454 continuum peaks, as well as 7 clumps in G11.11 with double peaked N_2H^+ lines. The two components have velocity offsets of only a few km/s. Since the hyperfine structure of N_2H^+ includes an optically thin component, we can exclude opacity and self absorption effects, a common feature in dense star-forming regions. The two independent velocity components within IRDC 18454 have already been reported by Beuther & Sridharan (2007); Beuther et al. (2012), and Ragan et al. (in prep.) find multiple velocity components toward G11.11. Combining our N_2H^+ Nobeyama data with PdBI observations at $\sim 4''$, Beuther et al. (2013) reveal multiple independent velocity components toward IRDC 18310-4. These are not resolved within the Nobeyama data alone at the spatial resolution of $18''$. Similar multi-component velocity signatures have been found in high spatial resolution images of dense cores in Cygnus-X (Csengeri et al. 2011a,b), and toward IRDCs by Bihr et al. (subm.). Therefore, it seems to be a common feature in high-mass star-forming regions.

Using radiative transfer calculations of collapsing high-mass star-forming regions, Smith et al. (2013) show that such double peaked line profiles may be produced by the superposition of infalling dense cores. Therefore, in high-resolution studies, which filter out the large scale emission, multiple cores along the line-of-sight can be detected. However, comparing our beam sizes of ~ 0.5 pc for IRDC 18454 and ~ 0.8 pc for G11.11 to typical sizes of cores below 0.1 pc, the larger-scale clump gas should may be dominating our signal. Therefore it is clear that multiple velocity components due to cores are more likely to be identified in high spatial resolution imaging. While IRDC 18454 is at the intersection of the spiral arm and the Galactic bar, and therefore exceptional in many aspects, G11.11 is likely a more typical high-mass star-forming region, similar to what has been simulated by Smith et al. (2009) and Smith et al. (2013). If the double peaked line profiles originate from two dense cores within our beam, as suggested by Smith et al. (2013), the cores within G11.11 would need to be extremely dense or large. Instead, it seems more realistic that we detect the gas of the clump as one velocity component, and the second component is produced by an embedded single core of high density contrast moving relative to its parent clump. For IRDC 18454 we find double velocity spectra even in-between the peak positions. This suggests that the components are coming from two overlapping sheets, close in velocity. It is unclear whether these sheets are interacting or not.

4.4. Accretion flows along filaments?

In Sect. 3.3 we presented the velocity structure of the 16 observed high-mass star-forming regions. As we described, 5 complexes have no velocity structure, while 6 regions have smooth large scale velocity gradients. The velocity structure of IRDC 18223 is more complex and does not fit into either of these categories. For 4 regions we lack the sensitivity to draw a conclusion.

Despite the two general appearances, the large scale velocity structure of the clumps is very diverse. In general, structures larger than 1 pc usually show some velocity fluctuations. These can be either steady and smooth, or pointing to separate entities. It is worth noting that the physical resolution of the N_2H^+ observations ranges from 0.1 pc to 1.0 pc, with an average of 0.3 pc for the $18''$Nobeyama beam, and 0.7 pc for the $46''$with MOPRA. Therefore, we are not able to resolve smaller structures, and the 1 pc limit is observationally set. In fact, velocity fluctuations on smaller scales are still likely. However, the observations show that on clump scale, some clumps do show gas motions, while others are kinematically more quiescent. High-resolution studies, e.g. Ragan et al. (2012b), have proven for some regions that on smaller scales gas motions continue.

In order to understand the velocity structure of complexes with smooth velocity transitions, Figure 10 through Fig. 16 visualize the velocity gradients along given lines. As it has been discussed in Sect. 3.3, our velocity map of IRDC 18151 consists of 2 larger structures, IRDC 18151-1 in the east, and IRDC 18151-2 and IRDC 18151-3 in the west. The overall changes within the eastern and western clump are ~ 0.5 km/s and ~ 1 km/s, respectively. However, while the velocity cut through the eastern clump shows hardly any variation, the western clump has a noticeable velocity gradient. To detect at least part of the gas at intermediate velocities, we smoothed the N_2H^+ to a velocity resolution of 0.4 km/s. Figure 12 shows the velocity profile across both clumps. While the western clump shows a slight velocity increase toward the east, the eastern clump shows no velocity gradient. Especially, both gradients seem not to match, and if they interact dynamically, the transition zone would need to be short. Therefore we conclude that both structures are individual components, but in the context of other dense gas tracers both seem to be embedded within the same cloud. If seen from a slightly different angle, the double velocity components discussed in Sect. 4.3 could well originate from such a structure.

4.4.1. Flows along G11.11

A clear smooth transition of the velocity we find toward the northern part of G11.11. Shown by the top profile in Fig. 14, between G11.11-1 and G11.11-12, the differences in velocity are below 0.5 km/s. Along the profile just south of G11.11-1, the velocity starts to increase, with higher velocities toward G11.11-2 and beyond. On the other hand, the profiles perpendicular to the filament, right panel of Fig. 14, have almost constant velocities. Only the profile closest to G11.11-1 has a velocity gradient. However, the filament has a bend right at the position of the profile. A profile perpendicular to the actual shape of the IRDC would have no velocity gradient. Therefore, we conclude that the velocity gradient is solely along the filament.

Both Tobin et al. (2012) (observationally), and Smith et al. (2013, numerically), suggest large-scale accretion flows along filaments on, and probably producing, central cores. They describe the expected observational signatures for filaments that are inclined from the plane of the sky. Imagine a cylinder with a

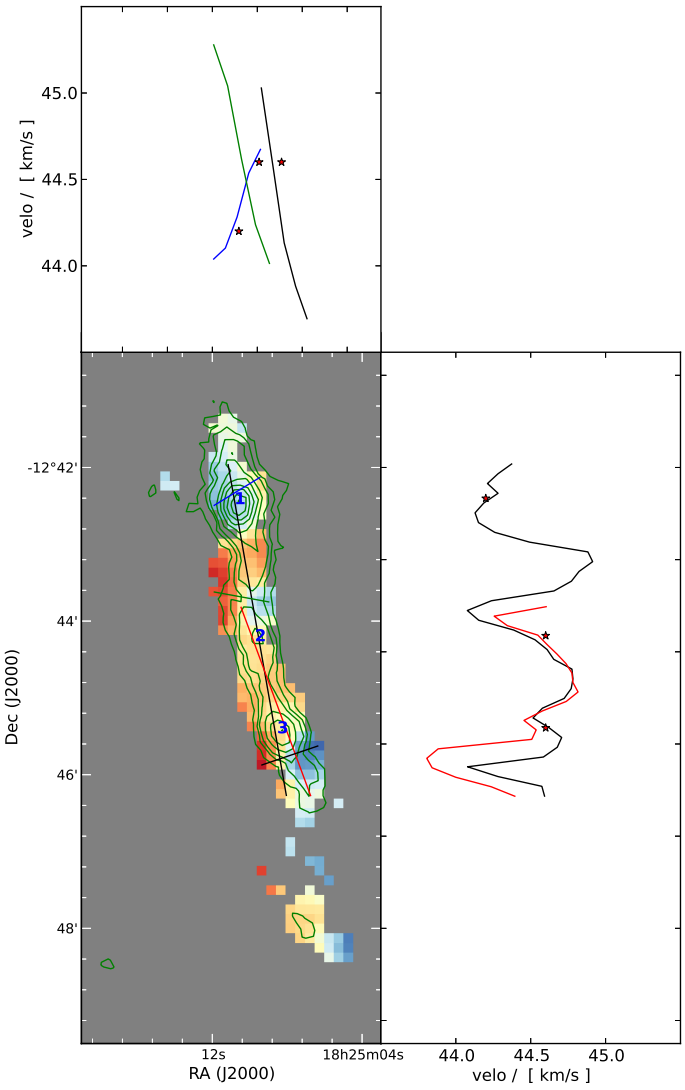

Fig. 10. Profile of the N_2H^+ velocity of IRDC 18223. The left panel shows the velocity map with contours from ATLASGAL superimposed (see also Fig. 1). The right and top panels show the velocity cuts along the lines marked on the velocity map. The stars mark the velocities of the clump peaks.

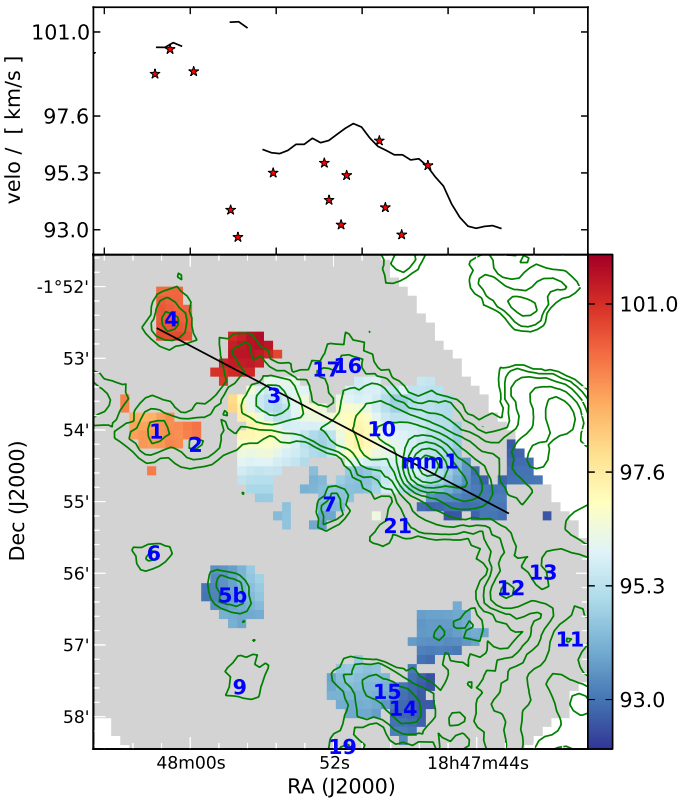

Fig. 11. Profile of the N_2H^+ velocity of IRDC 18454. The left panel shows the velocity map with contours from ATLASGAL superimposed (see also Fig. 1). The top panel shows the velocity cut along the line marked on the velocity map. The stars mark the velocities of the clump peaks.

central core, and material flowing onto the core from both sides at a constant velocity. For simplicity and without loss of generality, we put the central core at rest. Then, on each side of the central object the gas has a constant velocity along the filament. Since the gas is flowing in from both sides onto the core, a constant velocity is observed for both directions. The angle of the filament to the line-of-sight determines the observed velocity component. While Tobin et al. (2012) accounts for a gravitationally accelerated gas flow which should have a velocity jump at its center, the synthetical observations of high-mass star-forming regions performed by Smith et al. (2013) have a smooth transition. They also find local velocity variations, connected to smaller substructures.

Recalling the velocity structure we find for G11.11, our observations could be explained by such accretion flows along the filament. The filament would need to have an angle such that the south-east is further away from us than the north-west. The almost constant velocity over ~3 pc would be material moving toward G11.11-1, the most massive clump in the region. Just before G11.11-1, the velocity starts to increase and we observe the transition across the clump. Beyond G11.11-1, the gravitational potential of G11.11-2, the second most massive clump in this region, accretes material on its own, and accelerates the gas even further beyond the position of G11.11-1.

The scales we trace are an order of magnitude larger than what has been discussed by Smith et al. (2013) and our resolution is an order of magnitude worse. Because of the second dense clump, we do not observe the theoretically predicted pattern. The increase in velocity could also be explained by solid body rotation of part of the filament. Nevertheless, we propose an accretion flow along the filament as a possible explanation for the observed velocity pattern in G11.11. This view is supported by the fact that star-formation is most active at the center of the potential infall.

Consequently, if high-mass star formation is actively ongoing within G11.11-1, the material flow along the filament suggests continuous feeding of the mass reservoir from which forming stars can accrete.

4.4.2. Flows along IRDC 18308

A similar scenario could explain the velocity pattern along the IR dark part of IRDC 18308. The cut along the IRDC ending at the HMPO, see Fig. 13, shows only minor changes in velocity across the IRDC of ~2.5 pc length. In the vicinity of IRDC 18308-1, the velocity changes by almost 1 km/s on a short physical scale of only ~0.6 pc. The cut does leave a gap to the HMPO and does not fully close up in velocity. As described in

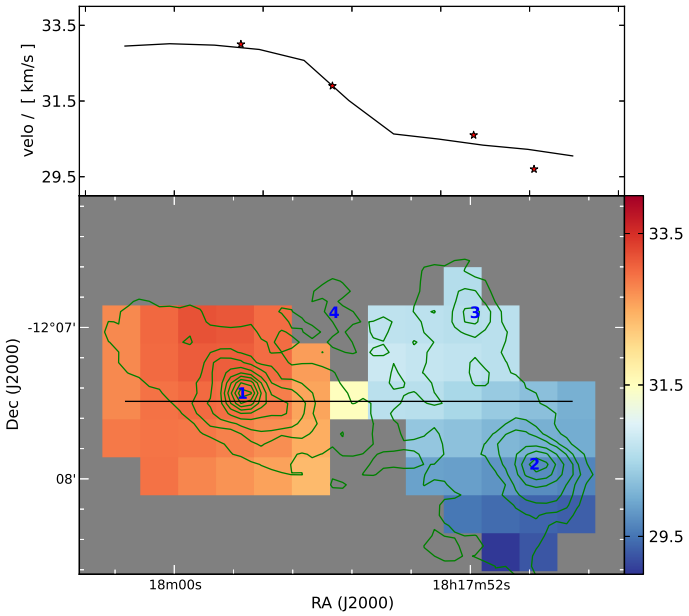

Fig. 12. Profile of the N_2H^+ velocity of IRDC 18151. The left panel shows the velocity map with contours from ATLASGAL superimposed (see also Fig. 3). The top panel shows the velocity cut along the line marked on the velocity map. The stars mark the velocities of the clump peaks.

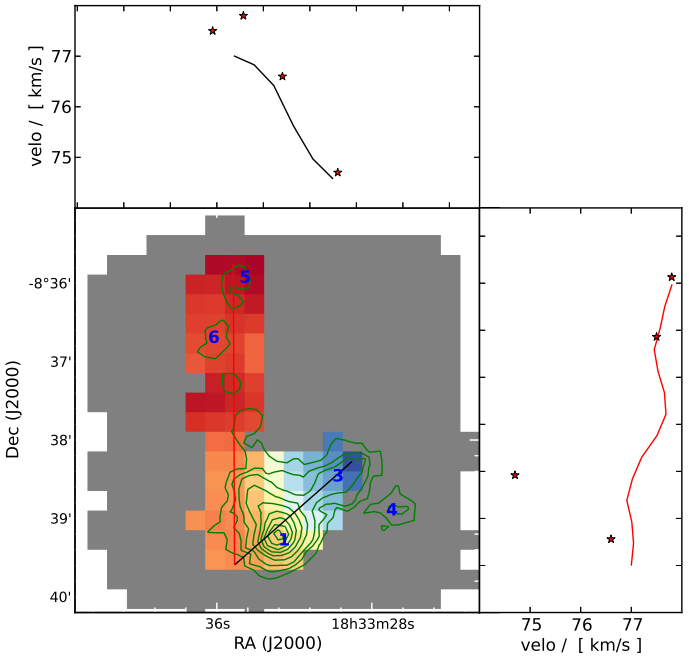

Fig. 13. Profile of the N_2H^+ velocity of IRDC 18308. The left panel shows the velocity map with contours from ATLASGAL superimposed (see also Fig. 3). The top and right panels show the velocity cuts along the lines marked on the velocity map. The stars mark the velocities of the clump peak.

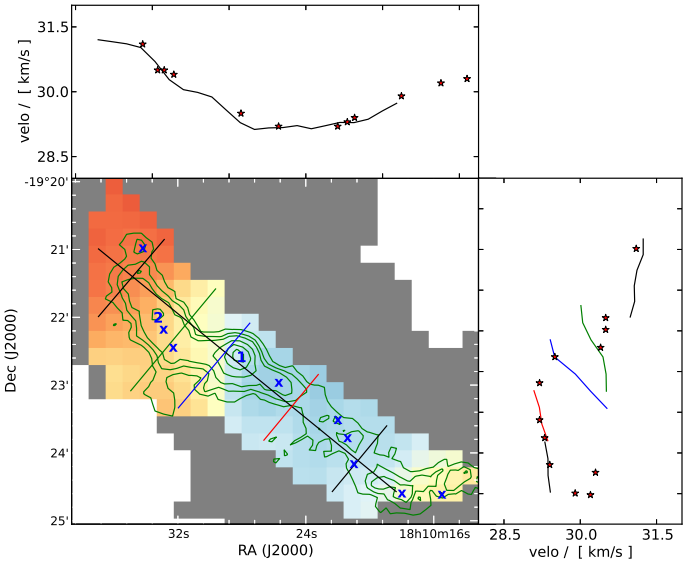

Fig. 14. Profile of the N_2H^+ velocity of the northern part of G11.11. The left panel shows the velocity map with contours from ATLASGAL superimposed (see also Fig. 2). The right and top panels show the velocity cuts along the lines marked on the velocity map. The stars mark the velocities of the clump peak.

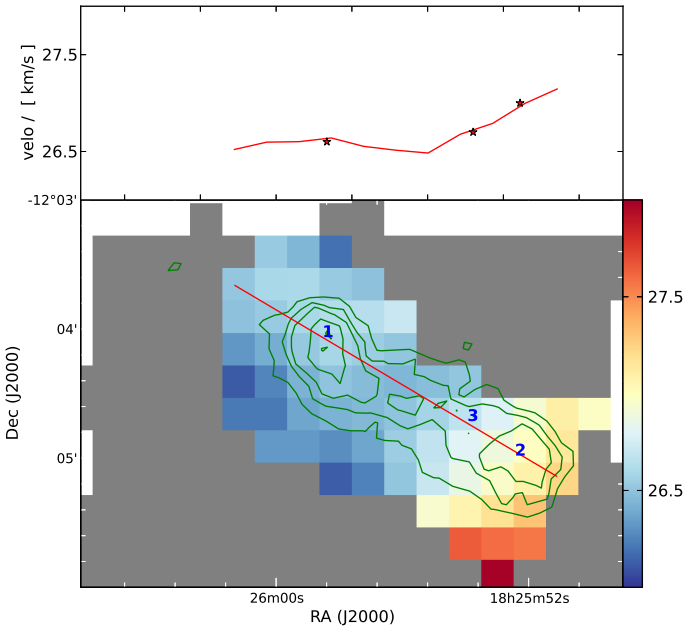

Fig. 15. Profile of the N_2H^+ velocity of G19.30. The left panel shows the velocity map with contours from ATLASGAL superimposed (see also Fig. 4). The top panel shows the velocity cut along the line marked on the velocity map. The stars mark the velocities of the clump peak.

Sect. 3.3, across the HMPO we find one of the largest velocity gradients in our sample, but the origin is unclear. One possible explanation that would produce a similar velocity profile is solid body rotation. In this picture, the knees at both ends of the profile would be caused by a transition from solid-body rotation to viscous rotation because of the lower densities in the outer regions. However, a full explanation would require a combination of hydrodynamic simulations with radiative transfer calculations. This is beyond the scope of this paper.

4.4.3. Flows along G19.30?

In G19.30, along the north-eastern part of the IRDC the velocity is constant over ~ 1 pc, and then it rises toward its other end. This suggests that the gas is flowing across G19.30-1, at the north-eastern end, through G19.30-3 towards G19.30-2. How-

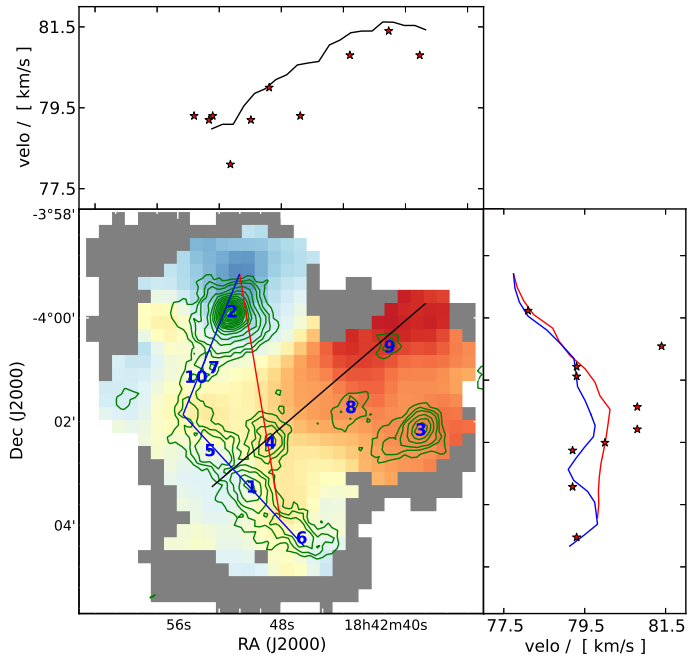

Fig. 16. Profile of the N_2H^+ velocity of G28.34. The left panel shows the velocity map with contours from ATLASGAL superimposed (see also Fig. 4). The top and right panels show the velocity cuts along the lines marked on the velocity map. The stars mark the velocities of the clump peaks.

ever, G19.30-1 is the most massive clump and therefore is potentially building the center of gravity. Therefore, the flow is opposite to the gravitational potential. The dust temperatures derived for the cores within G19.30 by Ragan et al. (2012a) are higher for the more massive clump G19.30-1, increasing our uncertainties on the mass. Nevertheless, even if we assume the higher dust temperature of 25 K for the whole G19.30-1 clump, and a temperature of 17 K for G19.30-2, both masses become of the same order. The additional clump G19.30-3 close to G19.30-2, is of similar mass as G19.30-2 and therefore increases the gravitational potential of the south-western end. Nevertheless, if our interpretation of a gas flow along the filament is correct, we do not find evidence that is it driven by gravity. Instead, this example could be interpreted as indication for a primordial origin of the flows, which lead to the formation of the clumps. Similar as for G11.11, the flows along the filaments within G19.30 and IRDC 18308 support the idea that the mass reservoir in high-mass star formation is continuously replenished.

4.4.4. The peculiar case of IRDC 18223

IRDC 18223 is filamentary, but with a more complex velocity structure than the previously discussed regions. Along the filament the velocity seems to be oscillating. The emission peaks of the southern clumps, IRDC 18223-2 and IRDC 18223-3, are at the same velocity of 44.6 km/s and in between the variations are minor. The peak of the clump IRDC 18223-1, harboring the HMPO IRAS 18223-1243, has a velocity of 44.2 km/s.

Perpendicular to the filament, we find three extreme velocity gradients, shown in Fig. 10. Although they are not going directly across the dust continuum emission peaks, each seems to be associated with a clump. A straight forward interpretation would be solid body rotation along the filament axis. However, as mentioned in Sect. 3.3, the two lower profiles indicate rotation in the opposite direction to the upper most profile. In Sect. 3.4 we discuss the possible influence of the powerful outflow within IRDC 18223-3 on the linewidth distribution. The same outflow could also alter the velocity distribution in its direct vicinity. Nevertheless, a change in rotation orientation along a single filament seems counter intuitive. For the massive filament DR21 within Cygnus X, (Schneider et al. 2010) find three velocity gradients perpendicular to the filament axis, with alternating directions. Suggesting turbulent colliding flows as origin of the filament, they interprete the velocity pattern as a remnant of the external flow motions.

Within IRDC 18223-3, on scales of 7″, Fallscheer et al. (2009) find a velocity gradient in N_2H^+ and CH_3OH, a high density and shocked gas tracer. They successfully model the CH_3OH velocity gradient with a rotating and infalling toroid, significantly larger than massive disk candidates (e.g. Cesaroni et al. 2005, for a contradictive example see Boley et al. 2012). However, the small scale velocity gradient presented in Fallscheer et al. (2009) has not only a slightly different orientation (by $\sim 45°$), but is also rotating in the counter direction compared to the gradient presented in Fig. 10. This implies that both gradients are independent and have different origins; the small scale infalling toroid is not connecting the large scale envelope to a possibly even smaller scaled disk. To first order this contradicts our previous statement of continuously feed clumps, because in this particular case, the large scale mass reservoir, or envelope, seems to be disconnected from the embedded HMPO. On the one hand, the velocity gradient seen in the large-scale gas might be confused by the outflow. As we discuss in Sec. 4.5.1, there is a clear correlation between the outflow and the linewidth distribution. Although N_2H^+ is not known to be commonly entrained in outflows, a similar correlation between the outflow and the velocity gradient seems not unlikely and could explain the change in velocity. Here we need to emphasize that the outflow direction and velocity gradient have an angle of almost 90°. On the other hand, it could well be that the accretion phase of IRDC 18223-3 has already stopped, and the large-scale envelope and the inner toroidal structure are decoupled. However, apart from its youth, it is counter-intuitive that the core first accreted from a rotating structure, and then developed an internal source rotating in the opposite direction. Therefore, we cannot offer a good explanation.

4.4.5. G28.34

A quite large and complicated region is G28.34. Most prominent and clear, it has a strong but smooth east to west velocity gradient. Along the velocity cut given in the top panel of Fig. 16, the velocity changes by 2.6 km/s over 7.1 pc. This results in a velocity gradient of 0.4 km/s/pc. The clump emission peaks within the south-eastern component of G28.34, namely G28.34-6, G28.34-1, and G28.34-5, all have the same velocity. However, as the velocity cut along them shows, the velocity of the dense gas between them seems to be oscillating, similar as found for IRDC 18223. Even further north, the emission peaks of G28.34-7, and G28.34-10 are still at the same velocity as the more southern clumps. Only north of those the velocity changes monotonically to smaller velocities on the order of a parsec.

From the smooth velocity transition from east to west, as well as the absence of double peaked N_2H^+ profiles, we conclude that all dense gas within the region is physically connected. However, to fully explain the observed velocity signatures of the complex dense gas morphology in G28.34, again numerical simulations are likely required.

4.4.6. IRDC 18454

The velocity analysis of IRDC 18454 is hampered by the fact that, as discussed in Sect. 4.3, several clumps show two independent velocity components at their peak position. Therefore, the mapped single velocities can either be the stronger of the two components, or an average of both. However, the large scale velocity gradient in east to west direction is clear and no artefact.

4.5. Discussion of the linewidth distribution

4.5.1. Outflow-induced turbulence

As we have described in Sect. 3.4, we find no correlation between the linewidth and neither the temperature, nor the H_2 column density.

The lack of a correlation between the temperature and the linewidth can be explained by the narrow thermal linewidth. At 20 K, the thermal line broadening of N_2H^+ is ~ 0.18 km/s (in FWHM), and ~ 0.16 km/s at 15 K. Compared to the observed linewidths of a few km/s, the non-thermal contribution dominates by far and temperature variations of a few K are smaller than our uncertainties of the measured FWHM.

Another possible contribution to the linewidth stems from turbulence. Since the clouds are close to virial equilibrium (see Fig. 9), the linewidth should scale with the column density. As mentioned in Sect. 3.4, we find no correlation between both quantities either.

Instead, the spatial resolution of the data prefers molecular outflows as the dominating contribution to the measured linewidths. Examining the N_2H^+ linewidth maps of each region, we find clear imprints of known outflows onto the linewidth distribution. A good example in this context is IRDC 18223-3, shown in Fig. 1. As we described already in Sect. 3.4, Fallscheer et al. (2009) reports the outflow direction in IRDC 18223-3 to be $\sim 135°$east of north. As Fig. 1 shows, we observe a line broadening along the same axis, with the highest velocities toward the edge. Due to the complex over-all velocity structure it is unclear whether the aligned velocity gradient is connected to the outflow as well. This would suggest the origin of the increased linewidth to be an unresolved velocity gradient. In contrast, shocks connected to bipolar outflows could enhance the turbulence, leading to broader lines. Another possible origin of a linewidth broadening toward the edge of clumps is provided by gravo-turbulent fragmentation, as described in Klessen et al. (2005). Therefore, we cannot assess the physical origin of the linewidth distribution. However, in this particular case the alignment of outflow and linewidth broadening suggests a direct connection.

A similarly clear correlation between the linewidth and outflow we find for IRDC 18102, for which the outflow direction has been observed by Beuther (priv. communication). For G11.11-1, Gómez et al. (2011) observed an outflow in east-west direction, or 90°east of north, while we find a significant line broadening similar to a bipolar outflow with an angle of $\sim 150°$east of north. Then, the angle between outflow and increase in linewidth is on the order of 60°. Therefore, a direct correlation between both observations is not mandatory, but in the context of the other regions possible.

Although the outflow has not been spatially resolved, the presence of SiO suggests the existence of an outflow toward the northern part of G15.05, while the southern part is SiO quiet (Linz et al., in prep.). Despite both the northern and southern part are IR dark even at 70 μm and the mass distribution peaks in between, the linewidth distribution in the north is significantly larger than in the south. A possible outflow could explain this linewidth distribution. Using SiO as general tracer of outflows, we find similar correspondence between increased linewidth and the presence of outflows for IRDC 18151-2, G19.30-1, and G19.30-2, and the eastern tip of G48.66.

No SiO has been found toward the IR dark part of IRDC 18182, IRDC 18182-2, and -4, for which the linewidths are among smallest within the region. However, in between the two clumps the linewidth broadens without the presence of known outflows. Therefore, additional factors have to be dominating here, for example superposition of the two independent velocity components.

The four pointings toward G28.34 covering SiO emission (Linz et al., in prep.) agree with the picture of an outflow dominated linewidth distribution. Nevertheless, due to the generally broad lines in that region, the variations are less pronounced compared to all other regions.

A particular case seems to be IRDC 18151-1. Fallscheer et al. (2011) reports an outflow connected to it with an angle of 315°east of north, but the linewidth is smaller than in IRDC 18151-2, 1.9 km/s compared to 3.1 km/s, respectively. In addition, it shows hardly any linewidth structure, and therefore differs from the other clumps, discussed so far.

Sridharan et al. (2002) and Sakai et al. (2010) find no SiO toward the two northern clumps of IRDC 18223, IRDC 18223-1, and IRDC 18223-2, but Sridharan et al. (2002) interpret the detection of CO line wings as an indication for an outflow. Therefore, the bipolar line broadening of the edges of IRDC 18223-1 (see Sect. 3.4) could be caused by an outflow. In contrast, the linewidth broadens toward the center of IRDC 18223-2. As the large-scale velocity gradient across IRDC 18223-2 is twice as big as for IRDC 18223-2, the line-broadening toward the center could be explained by unresolved small-scale velocity gradients. An alternative explanation for the broadening of the linewidth could be colliding flows, as discussed in Sec. 4.4.4. However, the velocity gradients are not perfectly aligned with the linewidth broadening which would be expected for colliding flows. We have no information on the SiO or other outflow tracers for IRDC 18310, and IRDC 18308.

4.5.2. The particular case IRDC 18454

The line width map of IRDC 18454 for a single component fit, given in Fig. 1, provides a combination over both detected velocity components (see Sec. 4.3). Therefore, it quantifies the internal motions within each beam. If the two velocity components originate from two sheets that are interacting, a combined linewidth is appropriate for the virial analysis. However, resolving the individual velocity components at the peak positions reduces the line width of the clumps significantly. They become more comparable to the other regions within this survey, but still, the resulting line widths are broader than the average line width that we find for all other clumps.

Combining our Nobeyama 45 m N_2H^+ single dish data with observations from the Plateau de Bure interferometer, Beuther et al. (2012) find two independent velocity components toward IRDC 18454-1 as well. While one component is consistent both in width and velocity with one of our velocity components, the other component is offset by ~ 1 km/s and twice as wide in the single-dish data. This difference can be explained by the better spatial resolution of $\sim 3.5''$of the PdBI observations. Although the two fragments, which Beuther et al. (2012) resolve within IRDC 18454-1, have very similar velocities, Fig. 7 in their paper shows a velocity spread of a few km/s over the Nobeyama

beam size of 18″. However, as already apparent from Fig. 1, the linewidth toward IRDC 18454-1 is particularly narrow compared to almost all other clumps within IRDC 18454. This can be explained partly by the absence of any 70 μm PACS source and its physical proximity to W43-mm1.

4.6. Discussion of the virial analysis

In context of the virial analysis, bound clumps are expected since most clumps show signs of ongoing early star formation or already have formed dense cores. Nevertheless, in globally unbound regions collapsing fragments could exist as well and form stars and clusters. As shown in Fig. 9, most clumps have larger virial masses than gas masses, or a slightly positive α index. However, within the errors all clumps could be gravitationally bound. Marked in the upper panel of Fig. 9 are all clumps associated with G28.34. As we will discuss in a second paper (Tackenberg et al, subm.), G28.34 is in a state of global infall. Nevertheless, despite their global contraction, their virial parameters are not different from the bulk of the distribution. This again emphasizes that a virial mass larger than the gas mass does not necessarily leads to dissolving clumps.

From Fig. 9 it appears that clumps without a PACS point source have a higher α parameter than clumps with a PACS point source. Furthermore, more massive clumps tend to have lower α parameters. Here it is worth noting that clumps with PACS point sources are on average more massive than clumps without embedded sources. In the context of both, flows along the filaments as discussed in this paper, and global infall as discuss in Tackenberg et al. (subm.), the mass of clumps increases over time. The difference between the populations with and without PACS point source then can be explained to first order by two simple scenarios. **(1)** The dense material that we observe today accumulated and fragmented on a very short time scale. Suggested by the competitive accretion scenario, some clump fragments accrete mass faster than others. Therefore, they became dense enough to start forming embedded sources earlier. **(2)** In an alternative scenario, not all clumps formed at the same time. Assuming a similar mass accretion rate for all clumps, the oldest clumps are today the densest ones, and already started forming stars.

5. Conclusions

Complementary to the existing *Herschel*/EPoS data, we mapped 17 massive star-forming regions in N_2H^+. Using CLUMPFIND on sub-mm data, mainly from the ATLASGAL survey at 870 μm, we extracted the clump population that our observations cover. Assuming a constant dust temperature of 20 K and the distances given in Ragan et al. (2012a), we calculated both peak column densities and clump masses. With only a few exception, the N_2H^+ and total gas column density distribution spatially agrees very well, but the N_2H^+ abundance varies in IRDCs by two orders of magnitude.

While five complexes show no velocity structure, six regions have smooth velocity gradients. For three regions the velocity structure is consistent with accretion flows along a filament. For DR 21 Schneider et al. (2010) find a velocity pattern very similar to what we find for IRDC 18223, and suggest that the velocity gradients perpendicular to the filament are remnants of colliding flow motions the filaments has formed from. For G28.34 and IRDC 18454, the velocity structure is very complex and a detailed modeling is beyond the scope of this work.

The linewidth distribution among the sources is very diverse, in particular, IRDC 18454 stands out. Even after resolving double-peaked line profiles and treating them carefully, its average linewidth is twice the value we find for all other regions. This could be explained by the location of IRDC 18454, which is associated with W43, a mini-starburst at the junction of a spiral arm and the Galactic bar. Sources for which the outflow direction is known show a line-broadening along the outflow. In addition, all clumps that have measured SiO show an increased linewidth, while the other clumps show hardly any variations. Therefore, the linewidth on the scale of clumps seems to be dominated by outflows and unresolved velocity gradients.

In conclusion, this study supports a very dynamic star-formation scenario. Clumps and cores accrete mass from the dense filaments. Whether the cores and filaments form from primordial flows, or the clump gravitational potential are the origin of the flows is unclear.

Acknowledgements. We are grateful to the referee for her/his constructive comments. S. E. R. is supported by grant RA 2158/1-1, which is part of the Deutsche Forschungsgemeinschaft priority program 1573 ("Physics of the Interstellar Medium"). PACS has been developed by a consortium of institutes led by MPE (Germany) and including UVIE (Austria); KU Leuven, CSL, IMEC (Belgium); CEA, LAM (France); MPIA (Germany); INAF-IFSI/OAA/OAP/OAT, LENS, SISSA (Italy); IAC (Spain). This development has been supported by the funding agencies BMVIT (Austria), ESA-PRODEX (Belgium), CEA/CNES (France), DLR (Germany), ASI/INAF (Italy), and CICYT/MCYT (Spain). SPIRE has been developed by a consortium of institutes led by Cardiff University (UK) and including Univ. Lethbridge (Canada); NAOC (China); CEA, LAM (France); IFSI, Univ. Padua (Italy); IAC (Spain); Stockholm Observatory (Sweden); Imperial College London, RAL, UCL-MSSL, UKATC, Univ. Sussex (UK); and Caltech, JPL, NHSC, Univ. Colorado (USA). This development has been supported by national funding agencies: CSA (Canada); NAOC (China); CEA, CNES, CNRS (France); ASI (Italy); MCINN (Spain); SNSB (Sweden); STFC (UK); and NASA (USA).

References

André, P., Men'shchikov, A., Bontemps, S., et al. 2010, A&A, 518, L102
Barnard, E. E. 1919, ApJ, 49, 1
Battersby, C., Bally, J., Ginsburg, A., et al. 2011, A&A, 535, A128
Benjamin, R. A., Churchwell, E., Babler, B. L., et al. 2003, PASP, 115, 953
Bertoldi, F. & McKee, C. F. 1992, ApJ, 395, 140
Beuther, H., Churchwell, E. B., McKee, C. F., & Tan, J. C. 2007, Protostars and Planets V, 165
Beuther, H., Linz, H., Tackenberg, J., et al. 2013, A&A, 553, A115
Beuther, H., Schilke, P., Menten, K. M., et al. 2002a, ApJ, 566, 945
Beuther, H., Schilke, P., Menten, K. M., et al. 2002b, in Astronomical Society of the Pacific Conference Series, Vol. 267, Hot Star Workshop III: The Earliest Phases of Massive Star Birth, ed. P. Crowther, 341–+
Beuther, H. & Sridharan, T. K. 2007, ApJ, 668, 348
Beuther, H., Sridharan, T. K., & Saito, M. 2005, ApJ, 634, L185
Beuther, H., Tackenberg, J., Linz, H., et al. 2012, A&A, 538, A11
Beuther, H., Zhang, Q., Sridharan, T. K., Lee, C.-F., & Zapata, L. A. 2006, A&A, 454, 221
Boley, P. A., Linz, H., van Boekel, R., et al. 2012, A&A, 547, A88
Bonnell, I. A., Vine, S. G., & Bate, M. R. 2004, MNRAS, 349, 735
Bronfman, L., Nyman, L.-A., & May, J. 1996, A&AS, 115, 81
Carey, S. J., Clark, F. O., Egan, M. P., et al. 1998, ApJ, 508, 721
Carey, S. J., Noriega-Crespo, A., Mizuno, D. R., et al. 2009, PASP, 121, 76
Cesaroni, R., Neri, R., Olmi, L., et al. 2005, A&A, 434, 1039
Clark, P. C., Glover, S. C. O., Klessen, R. S., & Bonnell, I. A. 2012, MNRAS, 424, 2599
Contreras, Y., Schuller, F., Urquhart, J. S., et al. 2013, A&A, 549, A45
Csengeri, T., Bontemps, S., Schneider, N., Motte, F., & Dib, S. 2011a, A&A, 527, A135
Csengeri, T., Bontemps, S., Schneider, N., et al. 2011b, ApJ, 740, L5
Egan, M. P., Price, S. D., Kraemer, K. E., et al. 2003, VizieR Online Data Catalog, 5114, 0
Egan, M. P., Shipman, R. F., Price, S. D., et al. 1998, ApJ, 494, L199
Fallscheer, C., Beuther, H., Sauter, J., Wolf, S., & Zhang, Q. 2011, ApJ, 729, 66
Fallscheer, C., Beuther, H., Zhang, Q., Keto, E., & Sridharan, T. K. 2009, A&A, 504, 127
Faúndez, S., Bronfman, L., Garay, G., et al. 2004, A&A, 426, 97
Goldsmith, P. F. 2001, ApJ, 557, 736

Gómez, L., Wyrowski, F., Pillai, T., Leurini, S., & Menten, K. M. 2011, A&A, 529, A161
Griffin, M. J., Abergel, A., Abreu, A., et al. 2010, A&A, 518, L3
Gritschneder, M., Lin, D. N. C., Murray, S. D., Yin, Q.-Z., & Gong, M.-N. 2012, ApJ, 745, 22
Hatchell, J. & van der Tak, F. F. S. 2003, A&A, 409, 589
Heitsch, F. & Hartmann, L. 2008, ApJ, 689, 290
Hennemann, M., Birkmann, S. M., Krause, O., & Lemke, D. 2008, A&A, 485, 753
Hennemann, M., Motte, F., Schneider, N., et al. 2012, A&A, 543, L3
Hildebrand, R. H. 1983, QJRAS, 24, 267
Hill, T., Motte, F., Didelon, P., et al. 2011, A&A, 533, A94
Johnstone, D., Fiege, J. D., Redman, R. O., Feldman, P. A., & Carey, S. J. 2003, ApJ, 588, L37
Jørgensen, J. K., Schöier, F. L., & van Dishoeck, E. F. 2004, A&A, 416, 603
Kessler, M. F., Steinz, J. A., Anderegg, M. E., et al. 1996, A&A, 315, L27
Klessen, R. S., Ballesteros-Paredes, J., Vázquez-Semadeni, E., & Durán-Rojas, C. 2005, ApJ, 620, 786
Ladd, N., Purcell, C., Wong, T., & Robertson, S. 2005, PASA, 22, 62
Launhardt, R., Stutz, A. M., Schmiedeke, A., et al. 2013, ArXiv e-prints
López-Sepulcre, A., Walmsley, C. M., Cesaroni, R., et al. 2011, A&A, 526, L2
Mac Low, M.-M. & Klessen, R. S. 2004, Reviews of Modern Physics, 76, 125
MacLaren, I., Richardson, K. M., & Wolfendale, A. W. 1988, ApJ, 333, 821
McKee, C. F. & Tan, J. C. 2003, ApJ, 585, 850
Men'shchikov, A., André, P., Didelon, P., et al. 2010, A&A, 518, L103
Molinari, S., Swinyard, B., Bally, J., et al. 2010, PASP, 122, 314
Motte, F., Schilke, P., & Lis, D. C. 2003, ApJ, 582, 277
Müller, H. S. P., Schlöder, F., Stutzki, J., & Winnewisser, G. 2005, Journal of Molecular Structure, 742, 215
Nguyen Luong, Q., Motte, F., Schuller, F., et al. 2011, A&A, 529, A41
Ossenkopf, V. & Henning, T. 1994, A&A, 291, 943
Ott, S. 2010, in Astronomical Society of the Pacific Conference Series, Vol. 434, Astronomical Data Analysis Software and Systems XIX, ed. Y. Mizumoto, K.-I. Morita, & M. Ohishi, 139
Perault, M., Omont, A., Simon, G., et al. 1996, A&A, 315, L165
Peretto, N., André, P., & Belloche, A. 2006, A&A, 445, 979
Peretto, N., André, P., Könyves, V., et al. 2012, A&A, 541, A63
Peretto, N. & Fuller, G. A. 2009, A&A, 505, 405
Peretto, N. & Fuller, G. A. 2010, ApJ, 723, 555
Peters, T., Banerjee, R., Klessen, R. S., et al. 2010, ApJ, 711, 1017
Pilbratt, G. L., Riedinger, J. R., Passvogel, T., et al. 2010, A&A, 518, L1
Pillai, T., Wyrowski, F., Carey, S. J., & Menten, K. M. 2006, A&A, 450, 569
Poglitsch, A., Waelkens, C., Geis, N., et al. 2010, A&A, 518, L2
Ragan, S., Henning, T., Krause, O., et al. 2012a, A&A, 547, A49
Ragan, S. E., Heitsch, F., Bergin, E. A., & Wilner, D. 2012b, ApJ, 746, 174
Roussel, H. 2012, ArXiv e-prints
Sakai, T., Sakai, N., Hirota, T., & Yamamoto, S. 2010, ApJ, 714, 1658
Sawada, T., Ikeda, N., Sunada, K., et al. 2008, PASJ, 60, 445
Schlingman, W. M., Shirley, Y. L., Schenk, D. E., et al. 2011, ApJS, 195, 14
Schneider, N., Csengeri, T., Bontemps, S., et al. 2010, A&A, 520, A49
Schöier, F. L., van der Tak, F. F. S., van Dishoeck, E. F., & Black, J. H. 2005, A&A, 432, 369
Schuller, F., Menten, K. M., Contreras, Y., et al. 2009, A&A, 504, 415
Smith, R. J., Longmore, S., & Bonnell, I. 2009, MNRAS, 400, 1775
Smith, R. J., Shetty, R., Beuther, H., Klessen, R. S., & Bonnell, I. A. 2013, ApJ, 771, 24
Sridharan, T. K., Beuther, H., Saito, M., Wyrowski, F., & Schilke, P. 2005, ApJ, 634, L57
Sridharan, T. K., Beuther, H., Schilke, P., Menten, K. M., & Wyrowski, F. 2002, ApJ, 566, 931
Sunada, K., Yamaguchi, C., Kuno, N., et al. 2000, in Astronomical Society of the Pacific Conference Series, Vol. 217, Imaging at Radio through Submillimeter Wavelengths, ed. J. G. Mangum & S. J. E. Radford, 19
Tielens, A. G. G. M. 2005, The Physics and Chemistry of the Interstellar Medium
Tobin, J. J., Hartmann, L., Bergin, E., et al. 2012, ApJ, 748, 16
Vasyunina, T., Linz, H., Henning, T., et al. 2009, A&A, 499, 149
Vasyunina, T., Linz, H., Henning, T., et al. 2011, A&A, 527, A88
Wang, Y., Zhang, Q., Pillai, T., Wyrowski, F., & Wu, Y. 2008, ApJ, 672, L33
Wienen, M., Wyrowski, F., Schuller, F., et al. 2012, A&A, 544, A146
Wilcock, L. A., Kirk, J. M., Stamatellos, D., et al. 2011, A&A, 526, A159+
Wilcock, L. A., Ward-Thompson, D., Kirk, J. M., et al. 2012, MNRAS, 422, 1071
Williams, J. P., de Geus, E. J., & Blitz, L. 1994, ApJ, 428, 693
Zinnecker, H. & Yorke, H. W. 2007, ARA&A, 45, 481

Table 6. 870 μm ATLASGAL clump properties

IRDC ident	RA	DEC	N_{H_2}	M_{dust}	R_{eff}	N_2H^+ abundance	$v_{N_2H^+}$	$\Delta v_{N_2H^+}$	aver. $\Delta v_{N_2H^+}$	$M_{vir,k=128}$	$M_{vir,k=190}$
	[°]	[°]	[10^{22} cm^{-2}]	[$M_\odot$]	[″]	[10^{12}]	[km/s]	[km/s]	[km/s]	[$M_\odot$]	[$M_\odot$]
18102	18 13 11.2	-18 00 06	11.2	1019.	57.1	3.0	21.7	3.2	2.7	680	1026
18151-1[1]	18 17 58.2	-12 07 26	32.2	677.	34.5	1.1	33.0	1.9	2.0	232	350
18151-2[1]	18 17 50.3	-12 07 54	20.4	524.	32.5	1.3	29.7	3.1	3.1	495	747
18151-3[1]	18 17 51.9	-12 06 54	6.6	184.	23.7	—	—	—	0.7	19	29
18151-4	18 17 55.7	-12 06 54	2.6	21.	9.0	—	—	—	3.0	128	193
18182-1[1]	18 21 09.2	-14 31 47	17.2	1032.	36.3	1.4	59.7	2.7	2.6	515	777
18182-2[7]	18 21 14.8	-14 33 04	2.9	382.	33.7	5.5	41.0	1.6	1.9	256	387
18182-4[7]	18 21 13.8	-14 34 11	1.6	100.	20.3	3.3	41.2	1.9	2.3	217	327
18223-1[1]	18 25 10.6	-12 42 24	8.1	975.	43.1	4.7	44.2	1.9	2.0	358	53
18223-3[1]	18 25 08.3	-12 45 23	4.9	449.	32.6	9.2	44.6	2.9	2.9	599	90
18223-2[1]	18 25 09.5	-12 44 11	3.3	374.	31.6	10.1	44.6	2.5	2.3	361	54
18306-1	18 33 23.6	-08 33 36	9.0	640.	32.3	4.8	78.0	2.7	2.7	536	809
18306-2	18 33 31.6	-08 32 36	2.0	107.	18.8	—	—	—	1.6	104	158
18308-1[1]	18 33 32.6	-08 39 16	8.2	1483.	40.3	3.9	76.6	3.0	3.4	1271	1916
18308-3[1]	18 33 29.8	-08 38 27	2.7	592.	33.7	6.5	74.7	2.7	3.0	796	1201
18308-4[1]	18 33 27.0	-08 38 53	1.6	81.	14.0	—	—	—	0.9	33	50
18308-5	18 33 34.6	-08 35 55	1.4	61.	12.7	10.6	77.8	1.8	1.6	83	125
18308-6	18 33 36.2	-08 36 41	1.4	57.	12.2	—	—	—	1.2	48	72
18310-1[1]	18 33 47.7	-08 23 51	6.5	1100.	33.2	9.0	83.2	1.9	2.4	566	854
18310-2[1]	18 33 43.7	-08 21 25	6.3	1236.	33.5	6.0	84.3	3.7	3.5	1209	1824
18310-4[1]	18 33 39.2	-08 21 11	2.6	346.	23.2	9.4	86.1	2.4	2.3	384	579
18310-3[1]	18 33 43.8	-08 22 13	1.5	221.	21.1	—	—	—	3.1	612	924
18337-4	18 36 37.0	-07 38 53	2.1	214.	26.0	—	—	—	2.9	497	749
18337-3[1]	18 36 18.2	-07 41 06	1.9	177.	24.9	5.4	56.0	2.6	2.6	371	560
18337-5	18 36 18.7	-07 41 43	1.7	137.	22.4	—	—	—	2.8	394	594
18337-2[1]	18 36 26.5	-07 41 15	1.5	44.	12.7	2.9	57.4	1.1	1.1	36	55
18454-mm1[4]	18 47 46.7	-01 54 26	80.8	16117.	50.6	2.6	95.6	5.4	6.3	6552	9880
18454-10	18 47 49.4	-01 53 59	8.4	3032.	40.1	12.5	96.6	7.3	6.0	4787	7219
18454-11	18 47 38.9	-01 56 55	8.0	2641.	38.2	—	—	—	—	—	—
18454-3[2]	18 47 55.4	-01 53 31	6.4	2089.	41.2	8.9	95.3	6.0	6.8	6161	9290
18454-12	18 47 42.2	-01 56 12	5.3	1358.	35.3	—	—	—	3.9	1729	2608
18454-13	18 47 40.4	-01 55 59	5.3	1704.	29.9	—	—	—	3.5	1204	1816
18454-14	18 47 48.2	-01 57 53	4.0	1095.	36.8	6.3	92.8	2.7	3.1	1165	1757
18454-15	18 47 49.1	-01 57 39	3.6	782.	27.7	7.5	93.9	3.2	3.3	994	1499
18454-1[2]	18 48 02.0	-01 54 01	3.4	608.	25.6	6.9	99.3	2.6	2.7	613	925
18454-4[2]	18 48 01.1	-01 52 27	3.3	443.	22.4	6.3	100.3	1.8	1.6	179	270
18454-2[2]	18 47 59.8	-01 54 12	3.3	666.	27.5	—	—	—	3.2	913	1377
18454-16	18 47 51.3	-01 53 06	2.5	354.	20.6	—	—	—	8.3	4660	7028
18454-5b[2]	18 47 57.7	-01 56 18	2.4	261.	18.2	7.5	93.8	2.6	2.7	428	646
18454-7[2]	18 47 52.3	-01 55 02	2.4	190.	15.9	10.4	94.2	2.6	2.7	373	563
18454-17	18 47 52.5	-01 53 09	2.1	240.	18.5	—	—	—	9.3	5237	7897
18454-6[2]	18 48 02.1	-01 55 43	1.9	115.	13.1	—	—	—	—	—	—
18454-19	18 47 51.6	-01 58 25	1.8	171.	16.6	—	—	—	2.7	399	603
18454-9[2]	18 47 57.3	-01 57 35	1.6	199.	18.2	—	—	—	2.6	395	596
18454-21	18 47 48.5	-01 55 20	1.6	212.	18.8	—	—	—	4.1	1048	1581
1930-1	18 25 58.4	-12 04 01	4.0	164.	30.1	10.8	26.6	2.7	2.6	299	451
1930-2	18 25 52.3	-12 04 56	2.9	93.	23.9	7.9	27.0	2.2	2.2	174	263
1930-3	18 25 53.8	-12 04 40	2.0	94.	26.2	8.9	26.7	2.1	2.1	171	257
G11.11-1[3]	18 10 28.1	-19 22 35	5.5	455.	30.1	5.3	29.5	1.9	1.9	234	352
G11.11-6[3]	18 10 07.0	-19 29 06	4.3	411.	31.4	4.7	29.8	1.7	1.9	237	358
G11.11-7[3]	18 10 06.5	-19 27 40	3.9	458.	31.0	2.9	29.4	2.3	2.4	363	547
G11.11-2[3]	18 10 33.3	-19 22 00	3.2	325.	29.3	8.0	30.5	1.9	2.0	249	376
G11.11-9	18 10 32.9	-19 22 11	3.0	83.	14.0	8.0	30.5	1.9	1.9	104	157

Table 6. continued.

IRDC ident	RA	DEC	N_{H_2}	M_{dust}	R_{eff}	$N_{N_2H^+}$	$v_{N_2H^+}$	$\Delta v_{N_2H^+}$	aver. $\Delta v_{N_2H^+}$	$M_{vir,k=128}$	$M_{vir,k=190}$
	[°]	[°]	[10^{22} cm^{-2}]	[$M_\odot$]	[″]	[10^{12}]	[km/s]	[km/s]	[km/s]	[$M_\odot$]	[$M_\odot$]
G11.11-10	18 10 05.2	-19 26 34	2.8	109.	18.2	—	—	—	2.2	178	268
G11.11-11	18 10 05.7	-19 26 46	2.7	130.	19.1	—	—	—	2.2	198	299
G11.11-12	18 10 18.0	-19 24 36	2.6	199.	25.1	7.8	29.9	1.7	1.7	158	238
G11.11-13	18 10 32.3	-19 22 27	2.5	237.	26.9	7.9	30.4	1.8	1.9	194	292
G11.11-14	18 10 05.4	-19 27 18	2.5	134.	19.1	—	—	—	2.3	205	309
G11.11-15	18 10 25.7	-19 22 58	2.5	166.	22.2	10.7	29.2	1.0	1.3	74	112
G11.11-16	18 10 04.8	-19 27 33	2.5	109.	18.5	—	—	—	2.0	158	238
G11.11-17	18 10 13.9	-19 24 17	2.1	106.	19.7	3.9	30.3	1.4	1.2	59	89
G11.11-18	18 10 21.4	-19 23 47	1.8	70.	16.3	8.5	29.3	1.6	1.6	86	130
G11.11-19	18 10 34.2	-19 20 59	1.7	73.	16.9	17.4	31.1	1.7	1.5	82	124
G11.11-20	18 10 22.0	-19 23 31	1.7	100.	20.3	8.2	29.2	1.6	1.6	110	166
G11.11-21	18 10 05.8	-19 26 05	1.6	75.	17.9	7.7	28.6	1.9	1.7	112	170
G11.11-22	18 10 21.0	-19 24 10	1.6	72.	17.3	10.7	29.4	1.6	1.7	102	154
G11.11-23	18 10 15.5	-19 24 37	1.5	37.	12.2	7.4	30.2	1.5	0.9	19	30
G13-4[5]	18 17 34.9	-17 06 43	4.0	370.	42.4	4.7	21.7	2.0	1.5	155	235
G13-3[5]	18 17 21.5	-17 09 18	2.0	70.	21.4	6.6	23.3	1.4	1.8	112	169
G13-1	18 17 19.2	-17 09 41	1.6	54.	19.7	—	—	—	3.5	379	571
G13-2	18 17 34.0	-17 05 27	1.5	20.	12.2	—	—	—	1.6	52	78
G1505	18 17 39.0	-15 48 53	1.4	36.	14.8	11.1	29.9	1.3	1.3	47	71
G2823-2[6]	18 42 51.9	-03 59 52	15.9	3136.	51.1	3.1	78.1	3.4	3.3	1509	2276
G2823-3	18 42 37.3	-04 02 09	5.7	890.	35.2	3.6	80.8	2.5	2.5	626	944
G2823-1[6]	18 42 50.4	-04 03 15	4.6	919.	37.4	7.7	79.2	3.4	3.5	1234	1861
G2823-4	18 42 48.9	-04 02 24	3.5	502.	28.9	8.1	80.0	2.7	3.0	722	1089
G2823-5	18 42 53.6	-04 02 33	3.0	771.	36.3	8.8	79.2	2.6	2.9	860	1298
G2823-6	18 42 46.5	-04 04 14	2.8	658.	34.2	5.4	79.3	3.0	3.1	883	1331
G2823-7	18 42 53.3	-04 00 57	1.9	118.	16.3	13.5	79.3	2.2	2.3	247	372
G2823-8	18 42 42.7	-04 01 43	1.8	176.	20.0	5.1	80.8	2.6	2.6	362	546
G2823-9	18 42 39.7	-04 00 33	1.8	85.	14.0	13.5	81.4	2.2	2.2	180	272
G2823-10	18 42 54.7	-04 01 08	1.7	145.	18.2	11.6	79.3	2.1	2.2	240	362

Notes: The columns are as follows: Clump identifier, as displayed in the figues; Names are adopted from [1]: Beuther et al. (2002b), [7]: Beuther et al. (2007), [2]: Beuther et al. (2012), [3]: Johnstone et al. (2003), [4]: Motte et al. (2003), [5]: Vasyunina et al. (2009), [6]: Wang et al. (2008)

Appendix A: Description of the linewidth distribution

IRDC 18223: We find a clear increase of the linewidth toward the center of IRDC 18223-2, but IRDC 18223-2 and -3 show an increase toward the edge.
IRDC 18310: In IRDC 18310-1 the linewidth increases not toward the sub-mm peak, but toward the detected PACS point sources within. IRDC 18310-4 is a 70 μm dark region and the the linewidth increases toward its edge. For in between IRDC 18310-2, -3, and -4 the measured increase in linewidth is due to two independent, overlapping components.
G11.11: While for the two main peaks of G11.11, G11.11-1, and G11.11-2, the linewidth increases prototypically toward its edges, the other clumps of the northern part shown in Fig. 2 show no such clear variation of the linewidth. The systematic offset in the mapping of the southern part of G11.11 does not allow a systematic study of the line parameters. Nevertheless, it is worth noting that the linewidth of the southern part is significantly larger than it is for the northern mapped part.
G15.05: No clumps detected at given column density threshold.
IRDC 18102: We find an increase in linewidth toward the sub-mm peak with its connected PACS point source. An additional broadening of the linewidth from the east to the south is prominent as well.
IRDC 18151: In IRDC 18151, IRDC 18151-2 has the largest linewidth with 3.1 km/s. However, it is known to have an outflow (Beuther & Sridharan 2007) which could explain the broad linewidth. Both brighter at PACS 70 μm (the associated PACS point source is with 4026 $L_\odot$ ~ 10 times more luminous than the one connected to IRDC 18151-2) and with a collimated outflow (Fallscheer et al. 2011) as well, thus IRDC 18151-1 has a linewidth of only 1.9 km/s. Along the dust continuum emission away from the center the linewidth increases again. However, the reported outflow is perpendicular to the dust continuum emission and therefore cannot explain the broadening of the linewidth. Despite its still luminous PACS point source of 184 $L_\odot$, IRDC 18151-3 has the smallest linewidth in this region with 0.7 km/s. That is consistent with the fact that López-Sepulcre et al. (2011) finds no outflows toward that source.
IRDC 18182: The well studied HMPO in the north with four outflows connected to it (Beuther et al. 2006) has an increasing linewidth toward its center. The region of interest, the IRDC in the south-east has its smallest linewidth at the peak of IRDC 18182-2. Although there is a PACS continuum source at its peak, Beuther & Sridharan (2007) detect no SiO toward that peak. The southern part of the IRDC, IRDC 18182-4 has slightly larger linewidth.
IRDC 18308: While the IR dark filament, connected to IRDC 18308-5 and IRDC 18308-6, has similar linewidth all along between 1 km/s and 2 km/s, the southern complex of IRDC 18308 has linewidths larger than 2.5 km/s. However, the peak of the linewidth is offset to the sub-mm peaks, but is north of IRDC 18308-1. It is interesting to not that the N_2H^+ column density is not aligned with the sub-mm continuum peak IRDC 18308-1, and the N_2H^+ linewidth peak is offset from the N_2H^+ column density peak. While the offset between the continuum and the N_2H^+ emission peak of $\sim 15''$could be explained by the pointing uncertainties, the offset between the column density peak and the linewidth peak of $\sim 42''$are not. Since the linewidth and N_2H^+ column density are measured from the same data, positional uncertainties are not an issue for their difference of $30''$. As described in 3.3, we checked for the peak of the linewidth map whether its spectrum is fit better by two independent N_2H^+ velocity components, but only find a single component. Due to the high velocity resolution of 0.1 km/s for that check we can exclude an additional component as cause of that broadening.
G19.30: The linewidth distribution in G19.30 peaks toward the two more massive sub-mm peaks G19.30-1, and -2, with an even further increase in linewidth north of G19.30-1. In between P1 and P2, the linewidth is smallest within G19.30-3, but still broad with ~ 2 km/s.
G28.34: The linewidth in G28.34 is in general very broad with $\Delta v > 2$ km/s with only few exceptions. It peaks toward the two main peaks G28.34-1, and -2 with linewidths of up to 3.5 km/s. The minimum in linewidth is found to be in between the two main peaks at G28.34-10 at an linewidth of 2.1 km/s. Using the maps smoothed to a velocity resolution of 0.4 km/s, we find even smaller linewidths along the IR dark filament beyond G28.34-9.
G48.66: The linewidths in G48 are narrow compared to other regions mapped within this sample. For the part where N_2H^+ is detected, the region with the highest absorption and the embedded but detected PACS sources, the velocity dispersion is broadest, and decreases along the filament to lower column densities.

Appendix A: Parameter maps of omitted regions

Appendix A.1: Nobeyama 45 m data

Appendix A.2: MOPRA data

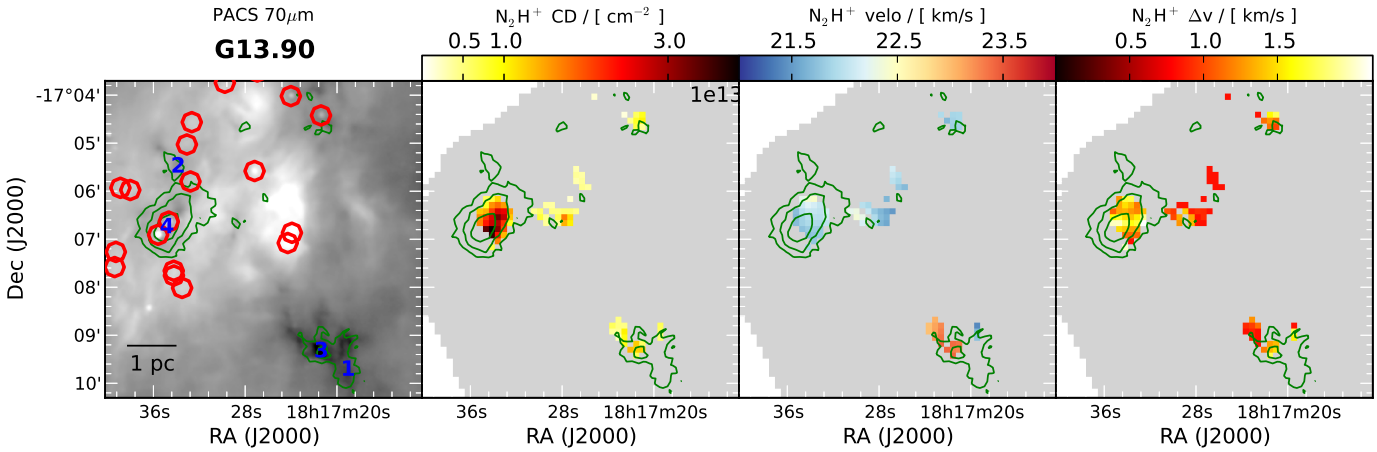

Fig. A.1. G13.90

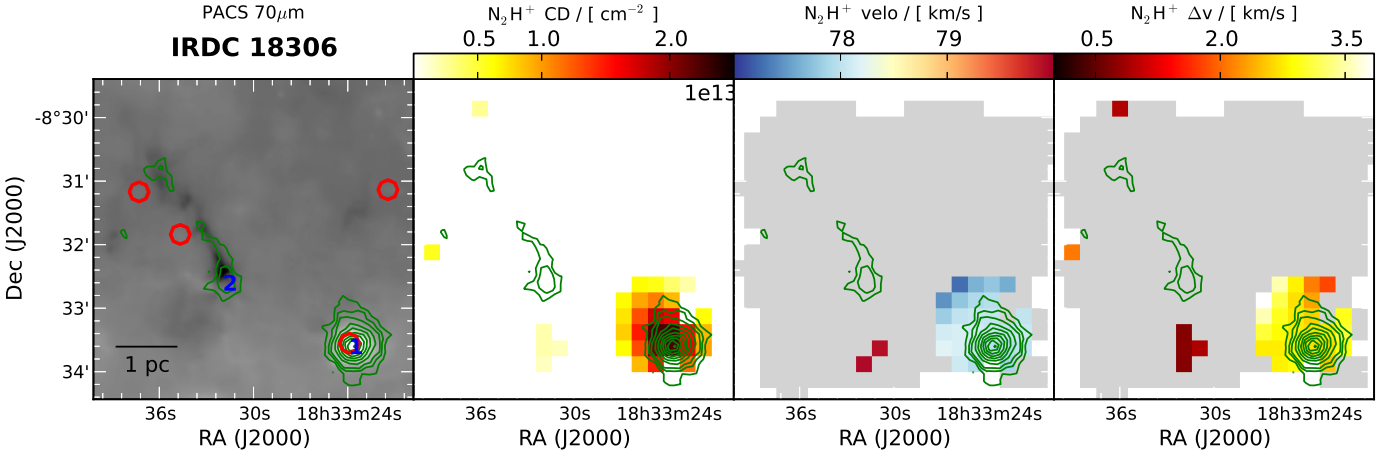

Fig. A.2. 18306

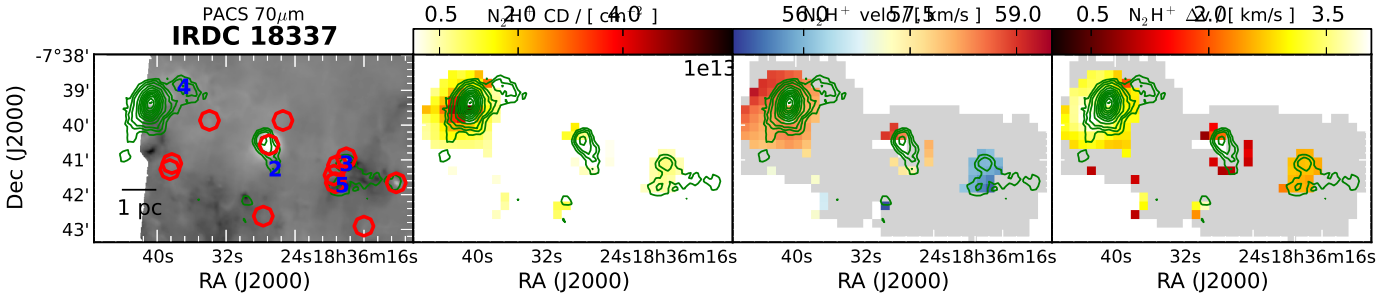

Fig. A.3. 18337